University of Brasília– UnB

Institute of Physics

Graduate program in Physics

Master Thesis

Nanoscale Investigation on the Structure and Stability of Nitrogen Enriched Carbon Nanodots Dispersions

By

Caio Matheus Ferreira

Supervisor

Prof. Dr. Jérôme Depeyrot

Brasília – DF

2024

Caio Matheus Ferreira

Nanoscale Investigation on the Structure and Stability of Nitrogen Enriched Carbon Nanodots Dispersions

A dissertation submitted in partial fulfillment of the requirements for the degree of EXPERIMENTAL PHYSICS (MSC) in the Institute of Physics, University of Brasilia.

Committee members :

- Prof. Jèrôme Depeyrot

- Prof. Luana Cristina Wouk

- Dra. Barbara Bianca Gerbelli

- Prof. Geraldo José da Silva

Brasília – DF

2024

“Investigação na Nanoescala da Estabilidade e Estrutura de Dispersões de Carbon Dots Enriquecidos por Nitrogênio”

By

Caio Matheus Ferreira de Carvalho

A dissertation submitted in partial fulfillment of the requirements for the degree of EXPERIMENTAL PHYSICS (MSC) in the Institute of Physics, University of Brasilia.

Thesis approved. Brasília, 5 de julho de 2024:

Prof. Jèrôme Depeyrot

Prof. Luana Cristina Wouk

Dra. Barbara Bianca Gerbelli

Prof. Geraldo José da Silva

“Não

Caio nessa hipocrisia

Da competição

Que tudo é corrida

Não

Malho nessa academia

Que exercita teu diploma

Enquanto teu sonho atrofia

Todo ser humano é capaz de magia

Uma vez revelada a verdade

Pra sempre rebeldia.”

Murica

Resumo

Dots de Carbono fazem parte da classe de nanomateriais zero-dimensionais que são importantes para várias aplicações na indústria de nano sensores, componentes fotoeletrônicos, na medicina e armazenamento de energia. Esses materiais ganharam espaço devido a sua síntese fácil e barata, suas propriedades óticas e excelente fotoluminescência. Neste contexto, o enriquecimento com nitrogênio nesses Dots pode melhorar ainda mais essas propriedades, e já foi mostrado que ele é capaz de mudar a estrutura interna e a superfície desses materiais, caracterizando os bem conhecidos Dots de Carbono Enriquecidos por Nitrogênio (N-CDs). Nesse trabalho, a estrutura dos N-CDs enquanto dispersos em meio aquoso foi investigada usando Espalhamento de Raios-X a Baixo Ângulo (SAXS) realizados em sincrotron e Espalhamento de Luz Dinâmico (DLS), discutindo o importante fenômeno de agregação que ocorre nesse sistema. Os resultados mostram que a quantidade de nitrogênio dentro dos N-CDs induz a formação de dois tipos de morfologia: fractais de massa para altas concentrações de nitrogênio e fractais de superfície para baixas concentrações de nitrogênio nos N-CDs. Além disso, um sistema complexo e hierárquico de agregados foi identificado nas dispersões de N-CDs, que são todos estáveis nas três condições de pH aqui consideradas: 2, 7 e 12. Os resultados foram interpretados usando a estrutura inicial do pó de N-CDs que foi investigado usando Difração de Raio-X (XRD), Microscopia de transmissão eletrônica de alta resolução (HRTEM) e SAXS, além dos mecanismos de carga da superfície que esses N-CDs tem. Os resultados são importantes para o melhoramento das Aplicações dos N-CDs, pois a relação entre as propriedades estruturais e óticas/eletrônicas ainda não são claras para esse sistema.

Palavras-chaves: Dots de Carbono, Dots de Carbono Enriquecidos por Nitrogênio, Espalhamento de Raios-X a Baixo Ângulo, Fractais de Massa, Fractais de Superfície, Estabilidade coloidal.

Abstract

Carbon dots are a class of 0-dimensional nanomaterials important for many applications such as nanomaterials for industry nanosensors as optoelectronic components, in the medical field, and in energy storage. They have gained space in the scientific community for their easy and cost-effective synthesis, optical properties, and outstanding photoluminescence. For this matter, carbon dots with nitrogen enrichment have been shown to change the inner and surface structures of the carbon dots, characterizing the well-established nitrogen-rich carbon dots (N-CDs). In this work, the structure of the N-CDs dispersed in an aqueous medium was investigated by using synchrotron Small-Angle X Ray Scattering (SAXS) and Dynamic Light Scattering (DLS), discussing the important phenomenon of aggregation that occurs in this system. The results show that the nitrogen content inside the N-CDs leads to two-types of morphology: mass fractals for high-nitrogen enrichment and surface fractals for low-nitrogen enrichment. Furthermore, complex and hierarchical aggregates were identified in the dispersion of N-CDs that are all stable in the pHs considered here: 2, 7, and 12. The results were interpreted using the initial structure of the N-CDs powders, which were initially investigated using X Ray Diffraction (XRD), High Resolution Transmission Electron Microscopy (HRTEM), and SAXS, as well as the surface charge mechanism that these N-CDs have. The results found can be helpful in enhancing the N-CDs applications since the relationship between the structural and optical/electronic properties is still not clear.

Keywords: Carbon-dots, Nitrogen-rich Carbon Dots, Small-angle X Ray Scattering, Mass Fractal, Surface Fractal, Colloidal Stability.

Acknowledgements

None of this work would have been possible in any level without the continuous support of my family, and for that I would like to thank my mother Adalgiza Helena and father Paulo Roberto for all the guidance, the long talks at the end of the days whenever I returned home stressed and insecure about life. In some way, this work is a result of their long time investment in me. My older sister Paula Helena and older brother Thiago Luis, since their successes and mistakes in their life were sources of great inspiration for my own, and my sister-and brother-in-law Jessica Guedes and Eric Meireles for the teachings and friendship, and to my nieces Manuela Maria Guedes and Rafaela Guedes. I love very deeply each one of you.

All I learned in life was taught thought the lessons of many important people. I would like to thank everyone from my second family: the scout group of João XXIII – 7º DF. Since I was little, they taught me what has become my moral compass, that true happiness comes from collective victories and that purpose in life comes from helping others. For all the love, laughs and great stories that we created together, I express my deepest gratitude. I would not be who I am if not for all of you.

From a very young age, curiosity was something that was always in my life, and the first time I arrived at University of Brasília, I found a place where I could not only explore fundamental problems of the universe, but actually try to tackle them. In this regard, I would like to that all my professors who gave me the tools to be a physicist, especially professors Letícia Gonçalves Nunes, Aleksandr Pinzul, Arsen Melikyan, Marco Cézar, Clovis Maia, Viktor Dodonov, Alexandre Dodonov, Junior Cruz, and Nádia Maria de Liz.

But the life of a scientist does not resume to the amount of tools that he learns, but also the expertise and way that they think, and to gain this much hard work and long hours of intense dedication and perseverance are necessary, that alone are nothing without good guidance. For that I would like to express my eternal gratitude to Professor Geraldo Jose da Silva, my first scientific father that taught me how to be and what it is to be a scientist.

Besides the hard work this thesis, the existential crises, and a sense of lost purpose that from time to time appears in life were only overcome with the help of friends I found in my undergraduate journey in physics. All my friends from CAFIS and from UnB – Arex, Ana Flavia, Diego, Didi, Luquinhas, Luiza Morais, Luizão, Isla, Clarencio, Nicolas (Nicboy), Grande Leo, Felipe Xererê, Carol, Dada, Raul Quartieri, Raul, Davide, Ricardinho, Macedinho, Heloisa, Nowras, Vitão, Isabella, Bia, Laura, Guilherme, Lucas, Daniel Bichão, and Adria; and to my childhood friend Murilo Cardoso for always having my back. I would like to thank you all for giving me the strength to keep going.

I would like to thank all the good friend I made in the laboratory at the Complex Fluid Group - Guilherme Gomide, Barbara Cavalcante, Deborah Liguiorini, Thiago Fuiza, Alex Fabiano, Rachel Bezerra, Cynara Kern, Elizabeth Andreoli, Leander Michels and others, for all the talks and insights while doing this thesis and during my undergraduate time.

During my master's degree, I found many important friends in the school I worked, I would like to thank Julia, Barbara, Brisa, Thaty, Bruno, Anne Karine, Nádyla, Kanso, Jales, Paulo Ferrari, Pedrinho and Daniel Peters, for their continuous support and friendship. Most especially I need to thank Alessandra Turra, for all her help and initial trust that she had in my teaching capabilities and for believing in me when there was no reason for doing so.

Lastly, I express my deepest gratitude to my supervisor professor Jèrôme Depeyrot, for all his help during this work, for challenging me with this scientific problem and believing that I was capable of doing this work and for always aiding me in whatever problem I had during my master's degree.

Contents

1. Introduction

Carbon dots are fascinating and very appealing materials due to their biocompatibility [1,2], tunable photoluminescence [3,4], cost-effective manufacturing [5], and environmentally friendly nature [6,7], propelling them as important nanomaterials for industry nanosensors [8,9], as optoelectronic components [10,11], in the medical field [12–15], and in energy storage [16]. This nanomaterial can be easily synthesized through either top-down or bottom-up routes that can use a wide variety of raw materials as synthesis precursors [17,18] and doping agents in their structure [19,20]. Consequently, three primary types of carbon dots can be formed: graphene quantum dots, carbon quantum dots, or carbonized polymer dots. In particular, carbon quantum dots (CDs) are described as 0-dimensional, quasi-spherical carbon-based nanoparticles with a small size of less than 10 nm that are water-soluble, have quantum confinement effects, and whose core structure contains a mixture of sp^2 and sp^3 carbons. Both their low crystallinity core and surface groups can be modified to meet specific applications. For the past decade, their synthesis and applications have been the focus of intense research [21,22].

Even though this novel material has gained so much space in the scientific community, some of their properties, especially their photoluminescence (PL), have not been completely understood, and the mechanisms behind them are still under debate, since factors such as the CDs nanoparticle size, their surface groups, and their core structure seem to all influence simultaneously their PL emission [23–25]. More recently, Ru et al. [26] drew attention to the important phenomenon of aggregation that occurs to CDs when they are synthesized and did a thorough discussion on various synthesis routes and their impact on the formation of the CDs nanoparticles/aggregates, a topic that has received comparatively far less attention them their PL. The discussion of their structural characteristics and morphology is very important since biomedical applications require that the CDs have a well-defined structure, especially in the environment where most of their applications are considered, i.e., while they are dispersed. This lack of clarity has inhibited a systematic improvement of the CDs applications since the relationship between the structural and optical/electronic properties are still not clear.

Nevertheless, reasonable progress has been made in establishing a correlation between the PL and the aggregation phenomenon in CDs dispersions with the introduction of Aggregation-Induced Quenching (AIQ) and Aggregation-Induced Emission (AIE) discussions in CD systems, a common topic in the study of the PL of organic luminophores [27]. To begin with, AIQ is the process that occurs for most CDs systems and is related to how the PL emission in high concentrations of fluorophore can effectively be reduced due to quenching and reabsorption effects [28], a phenomenon that can be mitigated by controlling the synthesis process with the introduction of new surface groups [29] and embedding the CDs in a suitable matrix [30,31]. On the other hand, CDs with AIE have a strong emission in aggregate form [32], and more notably, Liu et al. [33] prepared CDs with tannic acid and showed that if dispersed in tetrahydrofuran, their PL intensity increased linearly with the percentage of the solvent, which was correlated to the increase in the aggregate size with Dynamic Light Scattering (DLS) and Transmission Electron Microscopy (TEM) measurements.

While there is evidence in the literature correlating the aggregation phenomena and the corresponding PL of the CDs, a systematic approach to fully characterizing the CDs aggregate size and morphology while dispersed in a given solvent is still lacking. When it comes to examining the structure of dispersed nanoparticles, Small-Angle X-ray Scattering (SAXS) stands out as a reliable method for determining such parameters for nanoparticles in their native and realistic sample environments [34]. The difficulty involving the characterization of the individual nanoparticles and aggregates in dispersed CDs using SAXS is due to the poor scattering of the carbonic system; this hinders the distinction between the solvent and sample scattering, which ultimately requires the use of a synchrotron facility to obtain reliable data. As an example, by using time-resolved synchrotron SAXS and other spectroscopic measurements, Rigodanza et al. [35] was able to understand the nanoparticle formation mechanism of a polymer nitrogen based carbon dot during a hydrothermal synthesis and found a four-step process leading to a core-shell structure.

From the broad family of CDs, the ones obtained by the popular microwave decomposition are of great interest due to the capability of doping heteroatoms in their carbonaceous structure. In this context, the so-called nitrogen-rich carbon nanodots (N-CDs) are prepared by balancing the proportion of carbon and nitrogen molecular precursors in their synthesis, which can modify both the internal structure and surface groups of the N-CDs. These nanodots have been specially useful due to their large fluorescence quantum yields [4,19,36] and their structural and PL properties have already been extensively investigated [37,38]. On a further note, the colloidal stability of these N-CDs has been explored in a previous work [39], in which the surface charges of the nanoparticles were correlated to the medium’s pH with Zetametry and Potentiometric and Conductometric Titration measurements, revealing a greater stability in alkaline pH mainly due to the deprotonation of the carboxyl group present on the surface of the N-CDs, which helped to shed light on N-CDs interparticle interactions and in the interpretation of the PL emission.

In this context, the present work aims to further understand structural and morphological characteristics of N-CDs nanoparticles dispersed in an aqueous medium at acid, neutral, and alkaline pHs, all important environmental conditions for possible applications of these N-CDs. As a starting point, the structural characterization of the N-CDs powders was done in two specific conditions: as prepared by the synthesis (pristine) and after freeze drying the pristine powder (FD), using X-ray Diffraction (XRD), SAXS and TEM. When dispersed, the pristine N-CDs present some sedimentation as a bottom body is formed, especially in acid pH, and this sedimentation was quantified using time-resolved synchrotron SAXS measurements. Furthermore, better dispersibility is observed when using FD over pristine powders, and the individual characteristics of the N-CDs nanoparticles in both cases are investigated and compared. In addition, DLS experiments are also performed to evaluate the presence of large aggregates in the system. Finally, a centrifugation protocol is performed on the considered samples, and its impact on the nanoparticles colloidal stability that remain dispersed in also discussed with SAXS and Zeta potential measurements.

2. Materials and Methods

2.1. Synthesis of the Nitrogen-rich Carbon Dots and the Dispersion Preparation.

The nitrogen-rich carbon nanodots (N-CDs) studied here were synthesized following a bottom-up protocol with the microwave-induced thermal decomposition of organic precursors performed in a household microwave oven. This synthesis protocol is consolidated in the literature [4,19,37] as a direct, simple, and low-cost method consisting of just one step with ordinary equipment. Increasing the nitrogen content promotes not only promote changes in the crystalline structure, as will be discussed in Section 3.1, but also a shift of the PL emission from blue to green. The samples described and analyzed in the following sections were prepared by a group of collaborators from the physics department of the *Università degli Studi di Palermo* in Italy – Professor Fabrizio Messina and his team.

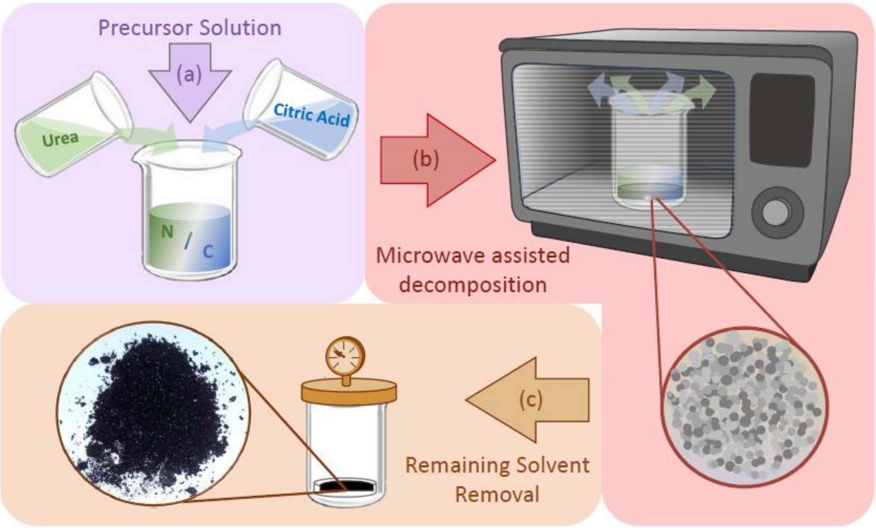

Figure 1 – Production procedure of nitrogen-rich carbon nanodots, that may be summarized as follows: (a) Preparation of the precursor solution by mixing urea and citric acid in a specific nitrogen-to-carbon molar ratio; (b) Decomposition of the solution using microwave assistance; and (c) Removal of the remaining solvent. The carbonization process of pure N-CDs results in the formation of a characteristic dark black powder, which is observed at the conclusion. Image taken from [40]

The used synthesis products that were used to produce the samples investigated were described by Sciortino et al. [4], in which urea (CH_4N_2O) is used as the nitrogen doping source and citric acid ($C_6H_8O_7$) adjusts the quantity of carbon. In this manner, a broad range of nitrogen and carbon molar ratios (N/C) can be explored by shifting the molar concentration of the reagents in the precursor solution, and [4] investigated N/C ratios from 0.14 till 1.5. The following grade reagents supplied by Sigma-Aldrich were used for the synthesis of the nanoparticles: citric acid monohydrate ($C_6H_8O_7{\cdot}H_2O$; M= 210.14 g/mol), urea (CH_4N_2O; M= 60.06 g/mol) and deionized water Type I (Millipore Milli-Q Gradient quality).

In this context, the N/C lower and upper bounds (0.14 and 0.74) were chosen to be investigated here in depth. In order to simplify the nomenclature of the samples the N/C = 0.14 will be referred to as CD1 and the N/C = 0.74 as CD7. The synthesis protocols of these samples are described as follows, and the step-by-step is given in Fig 1.

a) *Precursor solutions:* The organic aqueous precursor is prepared by fully dissolving in 10 ml of type 1 water 3 g of citric acid monohydrate and 0.39 g (3 g) of urea, resulting in a 0.14 (0.74) nominal atomic ratio of nitrogen and carbon is established.
b) Microwave-assisted decomposition: The solution is heated in a conventional household microwave oven (power set to 700 W) until the liquid phase is completely evaporated. The carbonization process is brief, taking only a few minutes, and results in the formation of a black powder. The yield can potentially achieve a maximum of 30% by weight of the original precursors.
c) c) Remaining Solvent Evaporation: Due to the high hygroscopic nature of the dark substance, it is subjected to vacuum drying for a duration of 90 minutes after being returned to room temperature. The end result is a high-quality, desiccated substance composed of clusters of N-CDs, as seen in Figure 1. Afterward, the powder may be evenly distributed in various aqueous solutions with carefully regulated physico-chemical characteristics.

The obtained powder is a strong hygroscopic black powder that was used in the experiments in two conditions: as obtained by the synthesis and after freeze-drying the powder. In the text, the powder condition prior to dispersion for both CD1 and CD7 N-CDs is referred to as *pristine* and *FD*, respectively.

To obtain the desired initial concentration, the investigated N-CDs were prepared by dispersing a certain amount of powder into the corresponding volume of aqueous solution, prepared at three different pHs – 2, 7, and 12 using type 1 water. The water's pH was adjusted by adding nitric acid for pH 2 and sodium hydroxide for pH 12. After mixing the components and mechanically agitating them, the dispersion is sonicated in a bath at a temperature of 65 ºC for three hours, and a uniform and homogeneous macroscopic visual aspect is obtained, which is later stored for further characterization. Furthermore, some of the prepared samples underwent centrifugation at 14000 rpm for 1 hour at room temperature, and an aliquot from the top and bottom phases was collected from the centrifuged samples and also utilized for the experiments.

2.2. Characterization

2.2.1. High Resolution Transmission Electron Microscopy

High-Resolution Transmission electron microscopy (HRTEM) images were obtained at the High Resolution Multiuser Laboratory (LabMic) of the Federal University of Goiás (UFG) using a JEM2100 electron microscope (JEOL) with an acceleration voltage of 200 kV, using a carbon type-A 400 mesh Cu substrate (TED PELLA) and bright field image mode. The pristine N-CDs were dispersed in deionized type 1 water and subsequently diluted in alcohol, being deposited over the substrate until dried before the experiment.

Figure 2. – Photograph of the JEM2100 electron microscope used for the experiments at LabMic. Photograph taken from [42]

2.2.2. X-ray diffraction

X-ray diffraction (XRD) is a nondestructive technique used to understand the crystalline structure of many materials, where an incident X ray wave hits the sample and reaches the detector at a given scattering angle 2θ. The theory of XRD is already very consolidated and can be found in detail in [43–45]. In this work the post-synthesis pristine dry powders were analyzed by XRD at the Central Analítica, Instituto de Química (CAIQ) of the University of Brasília (IQ-UnB). The measurements were conducted on a D8 Focus (Bruker) diffractometer with a Cu-Kα radiation source of λ = 0.154 nm. The samples were measured in a 10-90° range in 2θ with a 0.05° angle step at 0.1° min^{-1}, corresponding to a momentum transfer vector $\boldsymbol{q}$ ($q = \frac{4\pi \sin\theta}{\lambda}$) ranging from 7.1 to 57.6 nm^{-1}. From the broadening of the characteristic N-CDs diffraction peaks, Scherrer's equation (Eq. 1) can be used to estimate the mean N-CDs diameter:

$$D_{XRD} = \frac{k\lambda}{\beta \cos\theta} \qquad \textbf{(Eq. 1)}$$

where k is the dimensionless shape factor (0.9 for spheres), λ the x-ray beam wavelength, θ is half of the diffraction angle. To correctly account for the line broadening β, a Si standard was used to obtain the instrumental line broadening β_{ins} that is later deducted from the diffraction peak full width at half maximum (FWHM) as in:

$$\beta = \sqrt{FWHM^2 - {\beta_{\text{ins}}}^2}$$

2.2.3. Small Angle X Ray Scattering

Small- and Wide-angle X-ray Scattering (SAXS/WAXS) have been shown to be useful tools to examine the structure of nanomaterials [34]. To understand the morphology and structural characteristics of the N-CDs powders, SAXS/WAXS experiments were performed on the pristine and FD N-CDs powders at the Institute of Physics at the University of Brasília (IF-UnB) using a Xeuss 2.0 X-ray scattering equipment, with a Cu-Kα source of λ = 0.154 nm together with a two-dimensional detector (PILATUS3 R 200 K-A), as depicted in Fig 3. For SAXS geometry, the distance between the sample and the detector was 2.5 m, with q varying from 0.042 to 2.1 nm^{-1}. For WAXS geometry, the sample-to-detector distance was 0.55 m, with q varying from 0.18 to 9.8 nm^{-1}, and merging both geometries , the characteristic distances accessible ranges from 0.9 to 125 nm. All the powder samples used in the SAXS/WAXS experiments were mounted in a capillary and measured at room temperature, with no further physical-chemical modification to the powders. The scattering from the sample holder was later subtracted from the data following the usual normalization procedure [46].

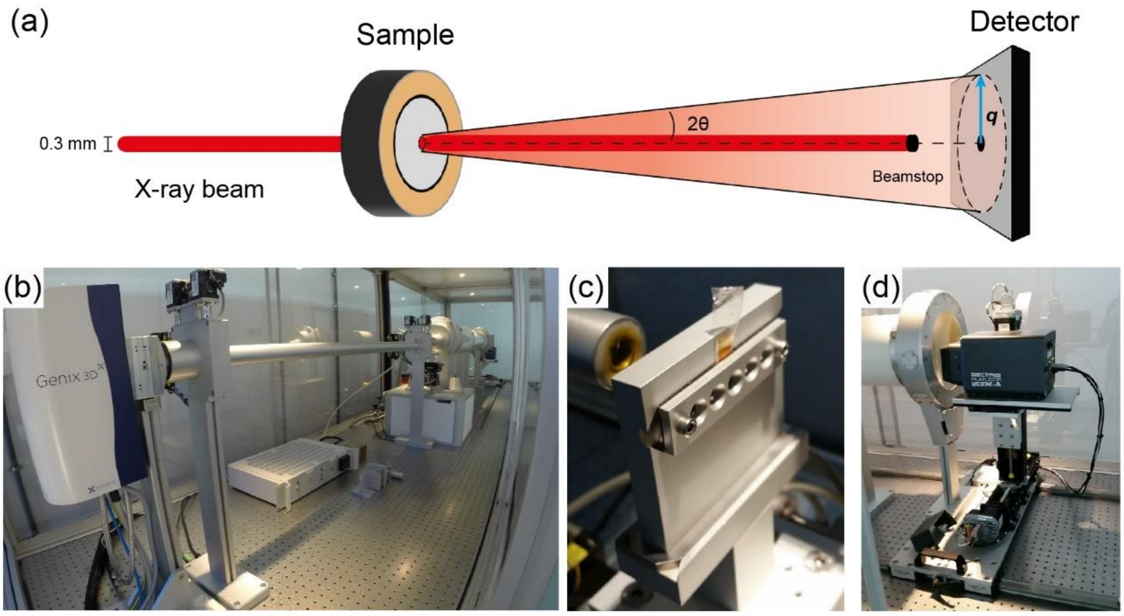

Figure 3. – Illustrations of the SAXS/WAXS experimental setup at IF-UnB. (a) Schematics of the SAXS experiment, the X-ray beam hits the sample and at a given sample-to-detector distance, the scattered waves reach the detector making a 2θ angle with respect to the direct beam, the latter is withdrawn from the scattering data with the use of the beamstop. (b) X-ray Cu-Kα source, (c) example of the sample holder used for the experiments and (d) the detector PILATUS3 R 200 K-A.

To measure the scattering of the N-CDs while dispersed, samples were prepared at an initial concentration of 30 g/L and synchrotron experiments were performed at the Centro Nacional de Pesquisas em Energia e Materiais (CNPEM) in the previous Laboratorio Nacional de Luz Sincrotron (LNLS) facility at beamline SAXS02 using a beam energy of 12 keV, which corresponds to a wavelength of 1.03 nm. The data was acquired in the 0.14 to 0.52 nm^{-1} q-range and were also subtracted from the scattering of the sample holder.

2.2.4. Modeling the SAXS intensity curves

SAXS intensity curves from complex systems are often hard to model due to multiple contributions that can be juxtaposed, especially using the traditional decoupling of the intensity into form and structure factors. For that reason, the use of shape-independent models can be an advantageous in revealing important and fundamental information concerning the size and morphology of the scattered structures, without the need for a precise description of the format and interaction of the nanoparticles.

In this work, an empirical model first introduced by Beaucage [48] is used. This model is useful to describe multilevel complex aggregate particles and hierarchical structures that are present in the same system [49–51], in which the Guinier and Porod regimes are unified in a single expression with a smooth transition between the two, thereby not adding new parameters other than those already used in the local fit. A two level Beaucage model can be described using the expression in Eq. 2.

$$\begin{aligned} I(q) = G\exp\left(-\frac{R_g^2 q^2}{3}\right) + B\exp\left(-\frac{R_S^2 q^2}{3}\right)\left(\frac{1}{q_{R_g}}\right)^P + G_S\exp\left(-\frac{R_S^2 q^2}{3}\right) \\ + B_S\left(\frac{1}{q_{R_S}}\right)^{P_S} + I_{\mathrm{Bkg}} \end{aligned} \qquad \textbf{(Eq. 2)}$$

Here G, B, G_S and B_S are scaling factors; R_g and R_S are the radii of gyration of the larger and smaller scattering sources, respectively, and can be related to the diameter (D) of an equivalent sphere as $D = 2R_g\sqrt{5/3}$. Similarly, P and P_S are the Porod exponents of the larger and smaller structures, and I_{Bkg} is an intensity background. Lastly, q_{R_g} and q_{R_S} are the factors that account for the smooth transition between both Guinier and Porod regimes of the large and small gyration radius and are defined in Eq. 3.

$$\begin{aligned} q_{R_g} &= \frac{q}{\left(\operatorname{erf}\left(\frac{qR_g}{\sqrt{6}}\right)\right)^3} \\ q_{R_S} &= \frac{q}{\left(\operatorname{erf}\left(\frac{qR_S}{\sqrt{6}}\right)\right)^3} \end{aligned} \qquad \textbf{(Eq. 3)}$$

This model will be referred to throughout the text as the Unified fit.

2.2.5. Dynamic Light Scattering and Zetametry

Dynamic Light Scattering (DLS) and Zeta potential measurements were performed using a ZetaSizer (model NanoZS 90, Malvern Panalytical) at the University of Brasilia – Campus Planaltina (UnB-FUP), with disposables DTS0012 and DTS1070 cells for DLS and Zeta, respectively. Since HNO_3 and $NaNO_3$ were each used to acidify and alkalinize the aqueous solution, the ionic strength was imposed to be 10^{-2} mol/L by adding sodium nitrate ($NaNO_3$) as a background electrolyte, in order to avoid the introduction of different ions to the system. The initial mass concentration used for both DLS and Zeta measurements was 1 g/L, and no further adjustments of the physical-chemical parameters were performed after combining the N-CDs with the suited medium. Temperature variation/gradient effects were evaded by performing all measurements at 25ºC.

For DLS, a He-Ne laser with a wavelength of 633 nm and 4 mW power was used, with the detector at a fixed position of 90º with respect to the incident light. In this setup, the magnitude of the scattering vector q is $1.871 \cdot 10^{-2}$ nm^{-1}. The DLS results are expressed as particle size distribution from the deconvolution of the measured intensity autocorrelation function ($g_2(\tau)$-1) of the samples by using a Non-Negatively Least Squares (NNLS) fitting algorithm provided by the software of the instrument (General Purpose). In this framework, the electric field correlation function ($g_1(\tau)$) is fitted to the optimal number of exponentials, generating an intensity weighted distribution of diffusion coefficients (D) as [52]:

$$g_1(\tau) = \int_0^{\infty} G(\Gamma) e^{-\Gamma\tau}\, d\Gamma \qquad \textbf{(Eq. 4)}$$

where $G(\Gamma)$ is the distribution of decay rates ($\Gamma = -Dq^2$). The sizes are obtained as hydrodynamic radius (R_H) calculated by the Stokes-Einstein equation (Eq. 5) using the viscosity of the medium (η) and the corresponding diffusion coefficient (D)

$$R_H = \frac{kT}{6\pi\eta D} \qquad \textbf{(Eq. 5)}$$

Now, the Zeta potential (ζ) is determined from the electrophoretic mobilities (μ) values obtained through Electrophoretic Light Scattering (ELS), by measuring the nanoparticle velocity using Laser Doppler Velocimetry (LDV). Then, the corresponding Zeta values are calculated using Henry’s equation with the Smoluchowski approximation (Eq. 6), since for the investigated system, the values of $\kappa R_H \gg 1$, based on the DLS results and the ionic strength of the medium (I):

$$\mu = \frac{\epsilon_0 \epsilon_r \zeta}{\eta} \qquad \textbf{(Eq. 6)}$$

Here, κ is the reciprocal of the Debye length as $\kappa = \left(\frac{\epsilon_0 \epsilon_r kT}{2N_A e^2 I}\right)^{1/2}$, N_A is the Avogadro constant, e is the elementary charge, ϵ_r is the dielectric constant of the solvent, and ϵ_0 is the vacuum electric permittivity. All the data presented was obtained by taking the average of triplicate measurements, for more accurate statistical analysis.

3. Results and Discussion

3.1. Characterization of the N-CDs powder

A starting point in order to understand the morphology of the N-CDs dispersed in aqueous media, is to have a good description of their structure in powder form. In that regard, XRD is especially useful to understand the structure of the core of the N-CDs [46], while HRTEM can reveal the size and morphology of the nanoparticles [19,37]. The results of these measurements done for both CD1 and CD7 samples in pristine powder form can be seen in Fig. 4(a, b).

The XRD data had a background signal that was subtracted by adjusting a polynomial function to the data as a baseline; after that, a single or double Lorentzian peak was fitted to the background subtracted data. Both CD1 and CD7 samples show amorphous diffraction peaks, characteristic of these types of carbonaceous materials [46], which are mainly related to the nanoparticles small size and their carbon/nitrogen ratio. Two diffraction peaks are seen for the CD1 sample owing to their lower nitrogen content, i.e., the graphitic structure is more predominant, while CD7 has only one diffraction peak as a result of the larger nitrogen content of this sample.

With the adjusted parameters of the Lorentzian fit, the crystallite size of both N-CDs can be estimated by using Eq 1; for CD1, values of (1.96 ± 0.05) nm and (1.97 ± 0.04) nm were found for the first and second peak respectively, revealing similar average size within the uncertainty. Likewise, for CD7, a crystallite size of (2.46 ± 0.03) nm was found, slightly larger than the size of CD1.

Other researchers have investigated the inner structure of the N-CDs [4,19,37], most notably through a combination of Raman and Fourier Transform of the HRTEM images [4] it has been shown that the carbon/nitrogen ratio has an impact on the N-CDs structure and their PL properties. Both CD1 and CD7 have hexagonal packing, but due to the lower nitrogen content in CD1, these samples have a more graphitic structure, namely C-graphite with space group P63/*mmc* – nº 194, and in this case nitrogen atoms are mostly defects inserted into the graphite core. On the other hand, CD7 has a β-C_3N_4 with space group P63/m – nº 176, due to the higher nitrogen enrichment, which strongly modifies both the core and surface structure of the nanoparticles.

Finally, the insets of Fig. 1(a, b) show the HRTEM images of the N-CDs. Despite the poor contrast of the samples, it is possible to verify the almost circular outline of the nanoparticles, which is their expected shape. The shape and corresponding structure of individual N-CDs nanoparticles are not expected to change with the FD process, as already shown in other studies with N-CDs synthesized with a similar method [47].

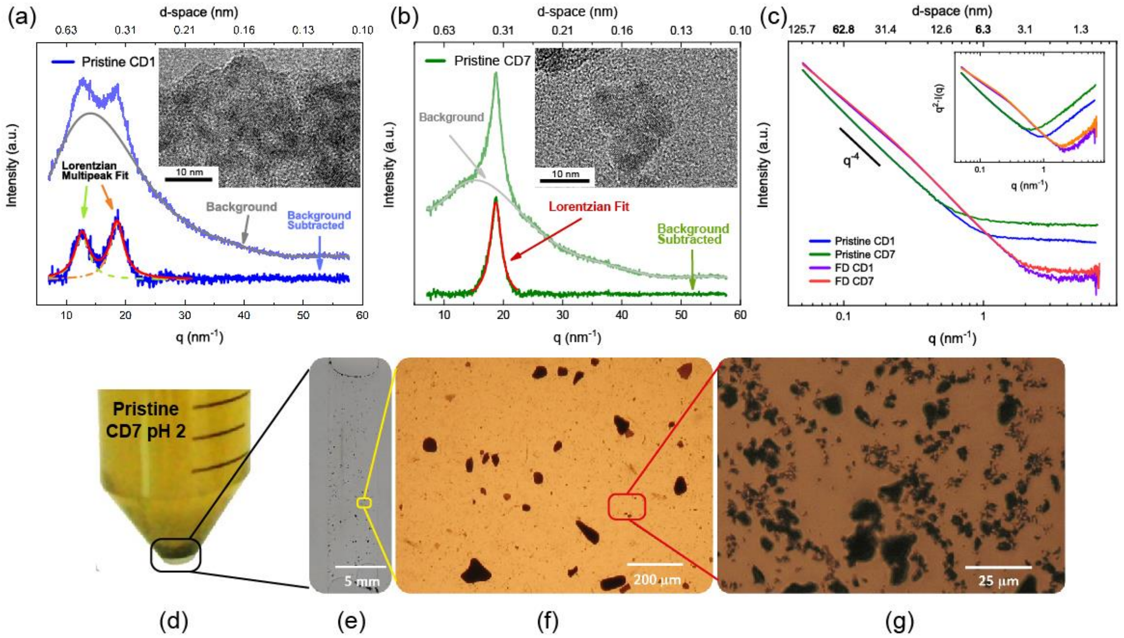

Figure 4. – Characterization of the N-CDs in powder form. XRD measurements of the pristine (a) CD1 and (b) CD7. The curves had their background removed and were fitted with one or two Lorentzian distributions; the insets on each diffractogram are HRTEM images of their respective N-CDs, and the scale corresponds to 10 nm. (c) SAXS measurements performed on both pristine and FD powders for CD1 and CD7. A line with -4 inclination was added alongside the curves as a guide to the eye, and the inset is the $q^2 \cdot I(q)$ (Kratky plot) curve for the same data. The d-space dimensions related to *q* for the XRD and SAXS/WAXS measurements are displayed at the top of the graphs. (d) Photograph of the pristine CD7 sample at an initial pH 2, highlighting the precipitate formed after homogenizing the sample. This precipitate was collected and dried on a microscope slide, and optical microscopy images were taken with (e) no objective lens, (f) a 5x, and (g) a 40x objective lens.

Complementary to the XRD and HRTEM data, SAXS/WAXS experiments can identify the interface of porous and granular materials of diverse sizes, ranging from nanopores to macropores [48,49]. To this end, SAXS of the pristine and FD N-CDs powder were performed, and the results are shown in Fig. 1(c). A -4 inclination is predominant in the majority of the *q* range of the experimental data for both pristine and FD samples, irrespective of the nitrogen content in the sample, but with FD samples having a larger predominance of the -4 inclination, all of them followed by a flat line in the high *q* region. Similar results were also obtained for N-

CDs obtained by hydrothermal synthesis with an intermediary N/C ration to the ones considered here [17].

This indicates that the N-CDs, in the considered q range, could be interpreted as made of a matrix that spans from large values of 120 nm to 10 nm for pristine powder without the presence of different hierarchical porous structures due to the transition from large to smaller interfaces. Such a description is also confirmed by looking at the $q^2 \cdot I(q)$ vs. q plot (see insert of Fig. 1(c)), which does not show inflections typical of porous/granular materials [50,51]. Even more, the matrix formed by the FD powder spans into even lower values of 3 nm, as seen in Fig. 1(c), which would indicate that the material now has more surface area, which can lead to better wetting of the matrix surface and better dispersibility [52,53].

We emphasize that near the q range that would correspond to the N-CDs particle size, no shift to another Porod law is seen, something that one would anticipate when transitioning from the N-CDs matrix to the individual nanoparticle. Thus, we suspect that in the considered q range, SAXS can’t distinguish the individual nanoparticles in powder form, probably due to their small size and how they are aggregated, showing that this type of N-CDs, synthesized by the bottom-up method, does not show different interfaces in powder form, in contrast to what is seen for other CDs in the literature, with larger nanoparticle sizes and prepared with other synthesis protocols and with the absence of nitrogen doping [51,54].

Having this description as a starting point, the pristine N-CDs were dispersed in mediums with different pH’s. N-CDs are highly water-soluble [36,55,56]. Their dispersibility is highly dependent on the medium’s pH [39] and for both CD1 and CD7 pristine powder prepared at pH 2, arguably the worst pH for particle dispersion, a bottom body is formed (e.g., see Fig. 1(d)) even after the homogenization described in Section 2.1, while for pH 12, less precipitate is formed. At the scale of Fig. 1(d), it is not clear if the precipitate is formed by the slow settling of clusters that could not be disaggregated from the powder or if it’s made of residue from the synthesis that simply is not dispersible. To investigate this, the precipitate was collected, dried, and observed under an optical microscope at different magnifications, as can be seen in Figs. 1(e, f, g). The presence of large dense aggregates with sizes ranging from 50–150 µm is evident, which are simply too heavy to stay dispersed, and interestingly with further magnification, less dense and smaller aggregates of 1–5 µm are also evident. The ampliation done to the bottom body, from Fig. 1(d) to Fig. 1(g), seems to show a fractal-like behavior to the flakes.

3.2. Sedimentation process

Furthermore, smaller particles that cannot be seen with the optical microscope can still sediment and contribute to the bottom body shown in Fig. 1(d). Thus, understanding the dynamics of this sedimentation process is important to probe the applicability of the N-CDs, especially for the extreme acid and alkaline mediums. For that, time-resolved synchrotron SAXS experiments were performed on the samples dispersed with the pristine nanoparticles in an initial 30 g·L^{-1} concentration at the moment they were prepared, considered here to be the time zero of our experiments. Immediately after preparation, shots were taken every minute for 60 minutes as the sedimentation occurred, and the results are shown in Fig. 2.

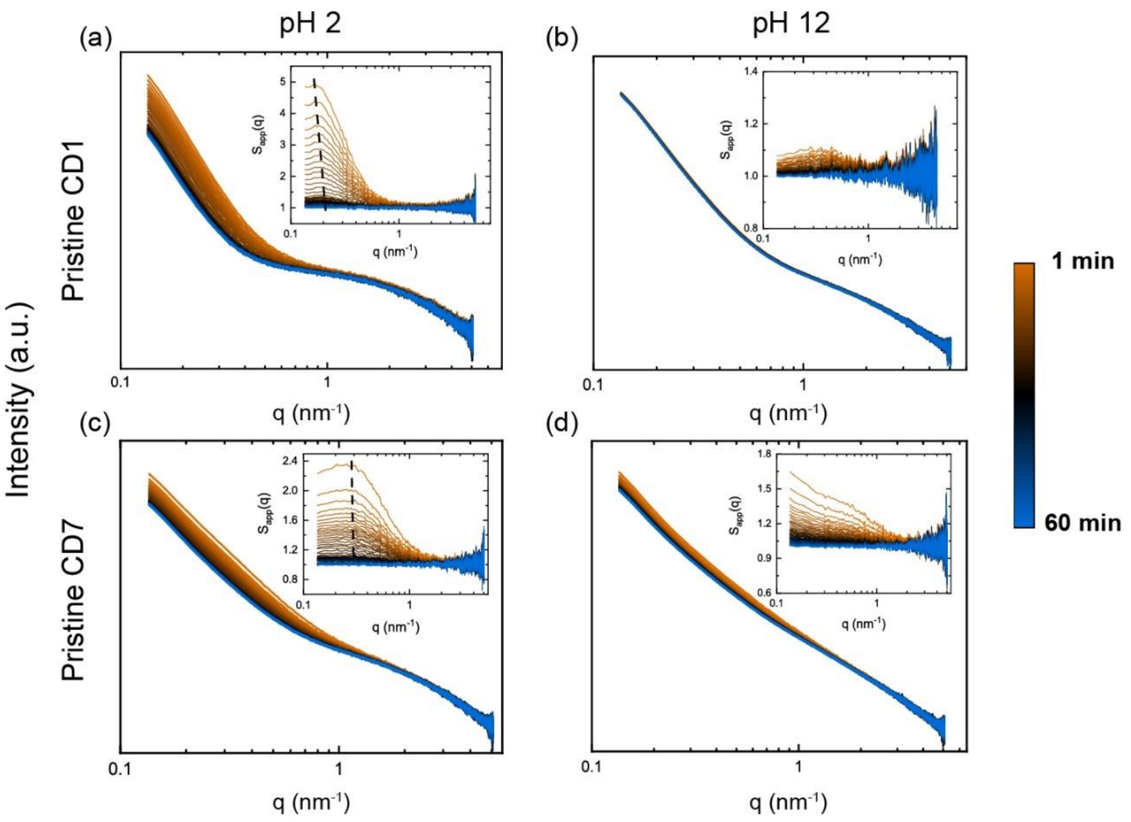

Figure 2. – Sedimentation dynamics of the N-CDs dispersions at an initial 30 g·L^{-1} concentration for pristine CD1 at pHs (a) 2 and (b) 12, and pristine CD7 at pHs (c) 2 and (d) 12. Time-resolved measurements were done by taking 60 shots of one minute each, right after the sample was agitated. The insets are the apparent structure factor ($S_{app}(q,t)$) of the measurement data, determined with respect to the last measurement at 60 min, with the corresponding d-spacing in the top. The black dotted lines are a guide to eye of the dynamics of the apparent peak as time evolves.

When inserted in the aqueous medium, the dominance of the -4 inclination seen in the powder measurements (see Fig. 1(c)) is broken down, and all the SAXS curves collected present a two-level structure with different inclinations at low and high q and a transition region in the middle, close to 1 nm^{-1}, both of which could be related, respectively, to large and small nanometric aggregates [57], smaller than the smallest flakes seen in Fig. 1(g). By-products of the microwave-induce synthesis could also contribute to the sedimentation seen, but as discussed in [35] from the SAXS pattern of the dialysate solutions taken from the reaction mixture after the formation of their CDs, these particles are too small to scatter and don't contribute to the SAXS scattering in the considered low-q region.

On first inspection, the scattering from the small aggregates in the high q region doesn't have significant changes as time passes for all four samples in Fig. 2, which indicates that these smaller structures are indeed more stable in the dispersion. At pH 12, both CD1 and CD7 in the measured q region present low to almost no evolution in the scattered intensity during the one hour measurement, showing that not only at pH 12 more nanoparticles are dispersed due to the smaller bottom body formed after mixing, but also that at this pH, both small and large aggregates that are present in the dispersion process are stable and remain dispersed in the medium. This is in complete agreement with the stability characterization done by Zetametry in a previous work [39], related to the surface charge mechanism of the N-CDs nanoparticles, which is mostly due to the deprotonation of carboxyl surface groups [19,39,58] with an increase pH, which favors greater particle stability due to a larger repulsion between the suspended structures.

However, at pH 2, the curves exhibit a significant intensity evolution in the low q region, related to the sedimentation process occurring in the larger aggregates in the sample. In order to quantify this sedimentation, an *effective experimental structure factor*: $S_{\text{app}}(q,t)$, is defined by dividing all the obtained curves by the final acquisition at t = 60 minutes (t_f), as in:

$$S_{\text{app}}(q,t) = \frac{I(q,t)}{I(q,t_f)}$$

$S_{\text{app}}(q,t)$ is shown as an inset for each curve in Fig. 2, and as can be seen, most of the intensity variation is in fact concentrated in the low q region. An apparent correlation peak, which here can be interpreted as a measure of the sedimentation of the larger aggregates with respect to the state where the sedimentation of these aggregates settled, decreases its intensity over time in the region around 20-40 nm for both pristine N-CDs in pH 2, as is evidenced by the black dotted line in these insets. On the other hand, for samples in pH 12 the $S_{\mathrm{app}}(q,t)$ does not show significant changes.

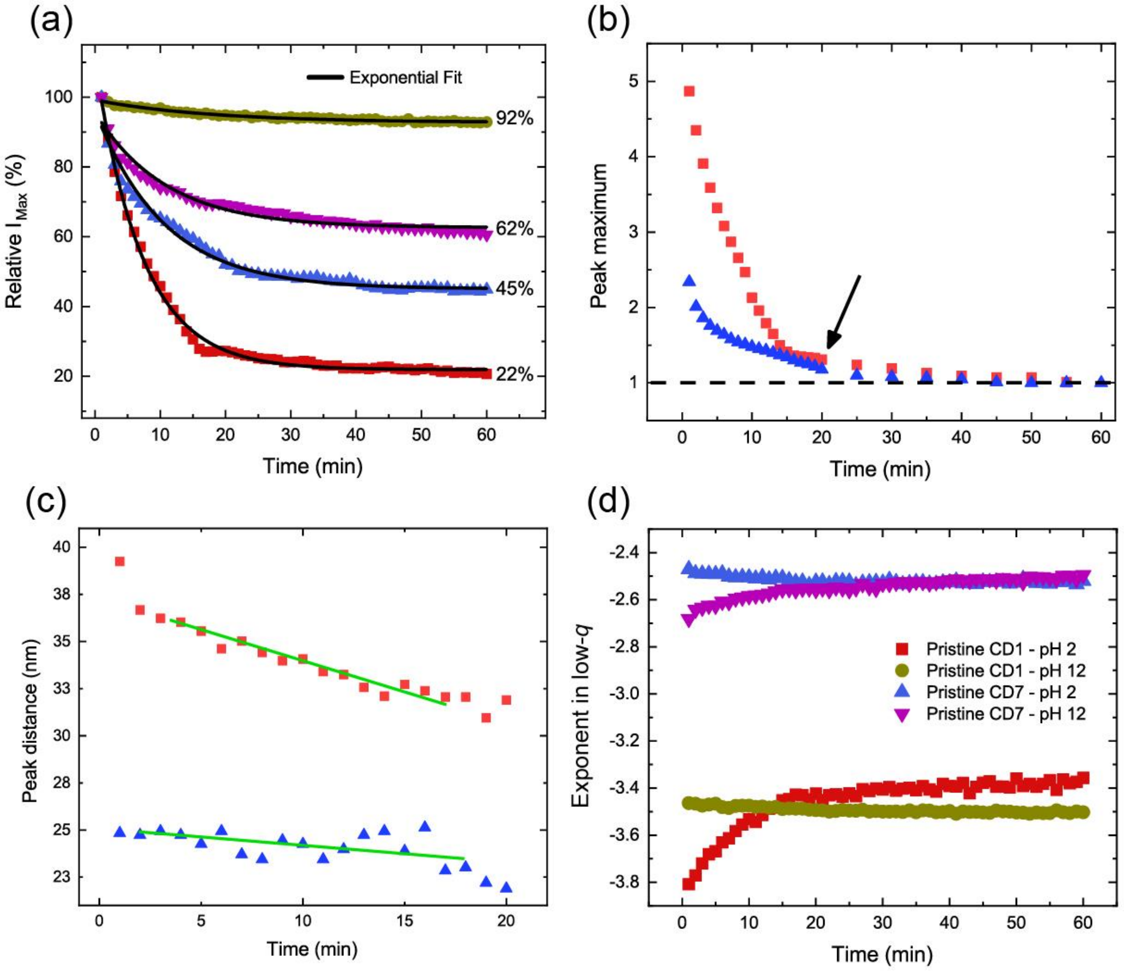

Figure 3. – Time evolution of important structural parameters, determined from the time-resolved measurements of the pristine CD1 and CD7 dispersions at pHs 2 and 12. (a) The relative maximum intensity (I_{Max}) of each curve at the lowest measured q value of 0.14 nm^{-1}; an exponential decay was adjusted to the data, and the residual percentual relative intensity is presented alongside each curve. (b) Peak maximum intensity of $S_{\mathrm{app}}(q)$ curves of the pH 2 samples; an arrow indicates the point where the sedimentation ceased, around 20 minutes after the beginning of the measurements. (c) The evolution of the peak distance of $S_{\mathrm{app}}(q)$ curves for the pH 2 samples; the green straight lines are guide to eye. (d) The evolution of the curve inclination in the Guinier region.

Most of the changes seen in the curves in Fig. 2 are related to concentration variations since the global format of the intensity curves doesn't change radically over time. Thus, one could expect that the aggregates are indeed precipitating, but some large aggregates still remain dispersed. To further investigate this dynamics, important empirical parameters extracted from the intensity curves, as functions of time, are shown in Fig. 3.

Firstly, it's hard to extrapolate to the scattering intensity at $I(q=0,t)$ to have a precise estimation of the particle volume fraction since the Guinier regime in the measured data range is not visible (i.e., $q \cdot R_g < 1.3$ inequality was not achieved [59]), thus the maximum scattering intensity (I_{Max}) was plotted as a function of time for a fixed q at 0.14 nm^{-1}, which would correspond to track the sedimentation for scattered nanoparticles of roughly 44 nm, and was further normalized by the maximum intensity at t = 1 minute, in order to highlight the decay behavior, that tends to stabilize as time evolves. Fig. 3(a) displays the results.

The intensity decay of all curves follows an exponential behavior, typical of first-order kinetics, and a good fit of the exponential decay model to the data further confirms that a sedimentation process is the most likely to be occurring. In this case, the intensity offset, shown alongside each curve, could be interpreted as an estimate of the percentage of scattering sources that remain present in the dispersion with respect to the initial suspended particles at time zero, showing that indeed, at pH 12, the dispersed N-CDs have greater stability, since 92% of the samples large aggregates tend to remain in the dispersion in the pristine CD1 sample, followed by CD7 with 62% also at pH 12. As opposed to the pristine N-CDs at pH 2, which showed that less than half of the initial large aggregates are still in the medium, the worst case being the pristine CD1 at pH 2, with only 22% of the aggregates remaining dispersed, the rest most likely being precipitated.

Furthermore, the evolution of the peak maximum value of $S_{\mathrm{app}}(q,t)$ is shown in Fig. 3(b) for both N-CDs at pH 2, which shows that the sedimentation process happens predominantly in the first 20 minutes, and after that, the system tends to settle as the intensity reaches values close to one. From the position of the apparent correlation's peak maximum, a plot of the correlation distance as a function of time is presented in Fig. 3(c), showing that this correlation distance is larger for pristine CD1 at pH 2 than for CD7 at the same pH, which could indicate that the aggregates seen in CD1 are further away when compared to CD7. Even more, this correlation distance shows small evolution for CD7 samples, as opposed to CD1, where this change is about 5-6 nm.

Lastly, Fig. 3(d) shows a close inspection of the evolution of the curve inclination in the low-q region, showing that the pristine CD1 and CD7 samples have different inclinations related to different fractal types of aggregates, which are respectively mass and surface fractals [60,61], that remain fairly stable as time evolves, except for the pristine CD1 at pH 2, which changes from -3.8 to -3.4 but still remains in the surface fractal regime. This minor change in the inclination of pristine CD1 at pH 2 could be related to the decrease in the average aggregate distance for the same sample in Fig. 3(c), since aggregates with morphology closer to the surface fractals rather than the ideal smooth sphere are the ones staying dispersed. As a result, the remaining aggregates have a more stable interaggregate distance that is slightly closer to each other.

In conclusion, we point out that the morphology of the large aggregates remains unchanged during sedimentation, which further corroborates the idea that the structure of the aggregates remains fairly the same as sedimentation occurs, i.e., no major flocculation is occurring in the investigated time range. However, it is worth noting that the nitrogen enrichment applied to the CDs does indeed modify their aggregation morphology inside the dispersion, a topic that will be explored in more detail in the next section.

3.3.Nanoscale organization

In search of a more efficient way to disperse the N-CDs, a FD process was done on the pristine powders, and with that, a better dispersibility of the N-CDs is readily observed in all pH’s worked here, which is expected since, as discussed previously, water can now better hydrate and break the dense nanoparticle matrix as these aggregated nanoparticle matrixes are spannable into smaller sizes (see Fig. 1(c)). Therefore, FD seems to be a good route to obtain more homogeneous N-CDs dispersions with little to no precipitate.

In principle, FD powder could lead to greater aggregation and mechanical stress, as is common in the lyophilization of nanoparticles for drug delivery systems [53,62], and Indriyati et. al. [52] have discussed the impact of FD in the drying of N-CDs powder prepared with a microwaved protocol as opposed to the pristine oven-dried powder normally produced, and differences in their PL and photothermal properties were observed that can be attributed to the different dispersibility of the N-CDs powders.

Therefore, in order to better understand the morphology and structure that these nanoparticles form when dispersed, in both pristine and FD form, synchrotron SAXS experiments were performed in dispersions prepared at an initial 30 $g \cdot L^{-1}$ concentration, a few days after its preparation. Fig. 4 displays the results.

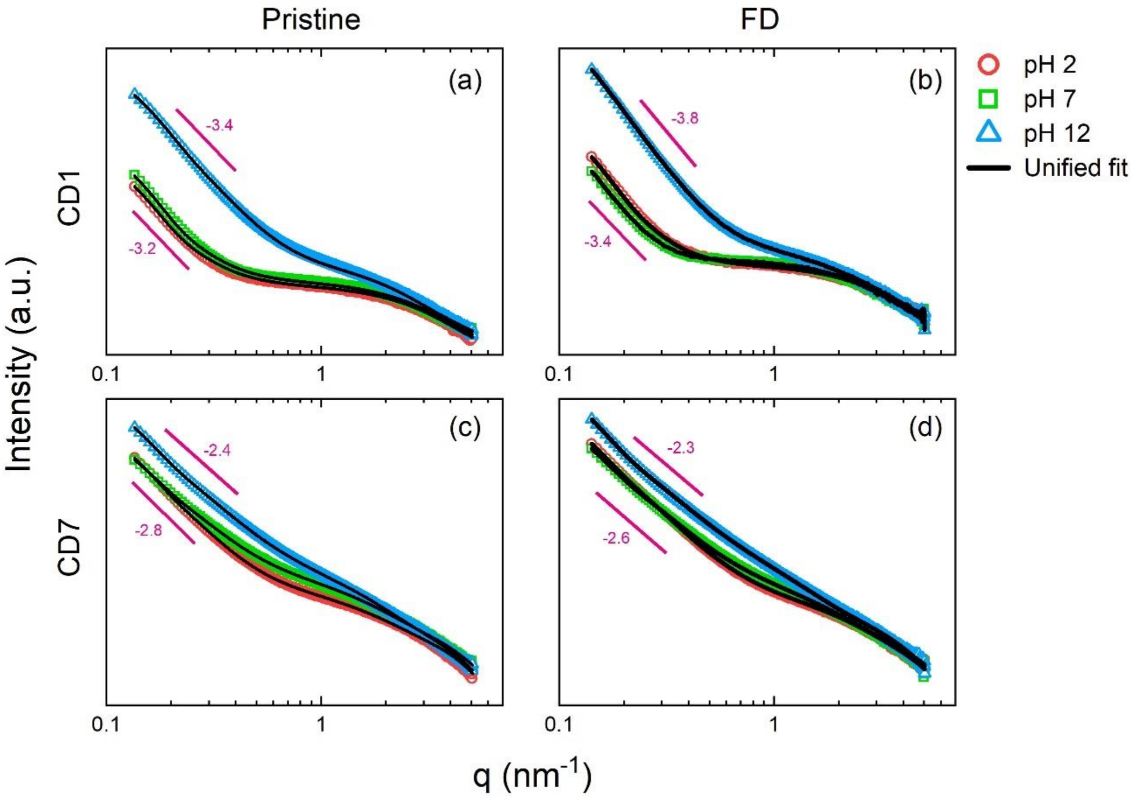

Figure 4. – SAXS intensity curves of the dispersions prepared with (a) pristine and (b) FD CD1, and (c) pristine and (d) FD CD7, all prepared at an initial 30 g·L^{-1} concentration and varying pH values of 2, 7, and 12. The black continuous line represents the adjusted Unified fit performed on all curves, and alongside the curves, a line with the corresponding inclination in the low-*q* region is shown.

On a first inspection, the curves inclination in the low-*q* region reveal two different types of large aggregates, irrespective of whether pristine or FD powder is used. For CD1, the inclination ranges from 3.2 to 3.4 for the pristine powder and 3.4 to 3.8 for the FD powder, with increasing values when going from acid to alkaline medium, which are typical values of surface fractals that present a close bulk morphology, but with an irregular surface [57]. Now for the CD7, the curve inclinations go from 2.4 to 2.8 for the pristine powder and 2.3 to 2.6 for the FD power, but now with decreasing values when going from acid to alkaline medium, whose values are typical of mass fractal systems that present a more open and spread morphology [63].

Such morphologies can be related to the nitrogen content inside each N-CDs. For the CD1 sample, the reduced nitrogen doping has less of an impact on the CDs inner core and their surface [4], leaving a more graphitic crystalline structure (see Fig. 1(a)), which in turn leads to a curve inclination closer to the bulk carbonic morphology of its precursor [64]. On the other hand, CD7 having more nitrogen doping affects not only the inner core of the CDs but also its surface, as more sites on the surface are occupied with the presence of oxidized nitrogen groups [19], which could be one of the causes to the mass fractal morphology. Even more, this change in inclinations when comparing the curves of pH 2 to 12 shows that the morphology of these large aggregates has a slight tunability with pH; however, it still stays inside the expected surface/mass aggregate range values, in agreement with the inclinations found for the sedimentation dynamics of the pristine powder (see Fig. 3(d)).

From the breakage of the -4 inclination seen for the N-CDs in powder form (see Fig. 1(c)) when the powder is added to a medium at a given initial pH to the mass/surface fractal inclinations seen in Fig. 4, it is reasonable to think that the wetting of the CDs matrix surface leads to its breaking into different pieces of small and large aggregates with different morphologies at the different pHs considered here. The amount of H^+ and OH^- clearly have an influence on the breakage of these nanoparticle matrix, and small differences in pristine and FD powder are also evident.

Starting from CD1, it appears that the deprotonation process of the carboxyl groups into carboxylate helps the development of irregularities on the surface of the bulk 3-dimensional carbonic surface of these N-CDs. In pH 2, less carboxyl sites are deprotonated, which leads to greater irregularities in the surface (i.e., a curve inclination closer to -3), since the interparticle repulsion is smaller and small N-CDs nanoparticles can adhere to the surface [65], while for pH 12, the interparticle repulsion is larger, making a tendency to stay near but not in the ideal inclination of the carbonic morphology, since now lesser particle-aggregate collisions are expected, especially for the FD powder, which has an inclination closer to -4. As for CD7, having fewer carboxyl groups than CD1, lead to the aggregates turning into a more spread configuration of mass fractals, which is reasonable since in pH 2, the deprotonation of the carboxyl groups is minimized, which leads to an increase to a higher inclination closer to -3, while for pH 12, the inclinations for the pristine and FD powder are closer to an aggregate with a polymer chain configuration [63]. One last point is that the curves in pH 2 and 7 have very similar scattering, which can be explained by the equilibrium pH that the N-CDs reach after preparation. In pH 2 and 12, the final pH is remarkably close to the initial, while for pH 7, this value tends to go to a more acidic value.

Finally, as discussed in the sedimentation process, all of the obtained SAXS curves present a two level scattering in high and low q, and in order to model this scattering, Eqs. (2) and (3) of the Unified Fit were adjusted to the experimental curves. A good match between the model and the experimental curves was obtained. The important fit parameters obtained are displayed for both pristine and FD powders in Table 1 for CD1 and Table 2 for CD7.

Table 1. – Values of the large and small diameter extracted from the Unified fit for the pristine and freeze dried CD1 dispersions, prepared at an initial 30 g·L^{-1} concentration.

Pristine CD1	**pH 2**	**pH 7**	**pH 12**
Large diameter (nm)	45.1 ± 2.2	45.0 ± 2.2	41.2 ± 0.6
Small diameter (nm)	1.53 ± 0.01	1.72 ± 0.01	2.09 ± 0.02

FD CD1	**pH 2**	**pH 7**	**pH 12**
Large diameter (nm)	45.1 ± 0.4	43.8 ± 0.4	47.6 ± 0.6
Small diameter (nm)	1.46 ± 0.01	1.62 ± 0.02	2.26 ± 0.02

Table 2. **-** Values of the large and small diameter extracted from the Unified fit for the pristine and freeze dried CD7 dispersions, prepared at an initial g·L^{-1} concentration.

Pristine CD7	**pH 2**	**pH 7**	**pH 12**
Large diameter (nm)	43.5 ± 1.4	41.5 ± 1.6	42.3 ± 1.3
Small diameter (nm)	1.99 ± 0.01	2.64 ± 0.02	2.61 ± 0.01

FD CD7	**pH 2**	**pH 7**	**pH 12**
Large diameter (nm)	43.5 ± 1.6	41.6 ± 1.2	42.6 ± 1.4
Small diameter (nm)	1.71 ± 0.01	2.28 ± 0.02	3.13 ± 0.08

The major differences between the curves in the low-*q* region seem to be related to concentration and morphological effects, since the average sizes related to the large aggregate diameter are equivalent for both CD1 and CD7 in all the pH's worked here, which is around 42 nm. Showing that in the considered *q*-range, the act of FD the pristine powder leads to the formation of size-equivalent large aggregates without leading to colloidal instability after redispersing the FD N-CDs [53].

Furthermore, in pH 12, all curves have more intense scattering in this region, which is an indication that more large aggregates are dispersed, which is in complete agreement with the N-CDs colloidal stability in the alkaline medium [39], since due to the deprotonation of the carboxyl groups, these aggregates are more stable due to stronger repulsion interactions, leaving more large aggregates dispersed in the medium.

But now, taking a look at the high-*q* region related to the values of the small diameter, the average size of CD7 is larger than that of CD1, a difference that was also seen with the values of their crystallite size in the XRD data (see Fig. 1(a, b)), and even more, these values tend to increase as the pH increases for both CD1 and CD7, prepared in both pristine and FD powder form, which shows that in the high-*q* region, the pH might has a slight tuning effect on the dispersed nanodots sizes.

Considering that in the high-*q* region of the SAXS data from the N-CDs powder (see Fig. 1(c)), we see the end of the Porod regime and the beginning of the flat line, after dispersing the powder, in this same *q*-region the structural level related to the smaller scattering source appears. As already pointed previously, most likely the wetting of the N-CDs breaks down the CDs matrix into pieces of different sizes, which go from the large aggregates that seem to have a similar average size but with different morphologies depending on the nitrogen content, to these smaller structures that change in size when the pH is increased. It is hard to specify if these smaller structures are indeed individual N-CDs or small aggregates consisting of a few nanoparticles, because no clear Porod interface is seen in the high-*q* region or even the development of a pH induced shell [35]. On top of that, the crystallite sizes taken from the XRD data (Fig. 1(a, b)) are not perfectly in agreement with the values found in Tables 1 and 2 for the smaller diameter, especially since for XRD these values are average sizes that do not take into account the polydispersion of this system, which other studies have already confirmed that a large polydispersity index is expected since a wide range of sizes ranging from 1 to 5 nm [19,37] for the individual N-CDs particles are visible.

Nonetheless, we can clearly see a preference for larger sizes related to the smaller structures in pH 12, and in the case of using the FD powder, these values are even larger in the alkaline pH, showing that both larger and smaller aggregates of N-CDs are stable at the considered pHs, and not all nanoparticles necessarily reaggregate with the larger aggregates.

Despite the fact that the SAXS data in Fig. 4 was acquired after the sedimentation ceased, it is possible that there are actually larger aggregates in the N-CDs dispersion, yet they are still smaller than the smallest flakes observed in Figure 1(g). In order to investigate this, dispersions were prepared using the same pristine and FD powder, but with a lower concentration of 1 g·L^{-1}. Afterwards, DLS experiments were performed at the same pH conditions. Fig. 5 displays the results.

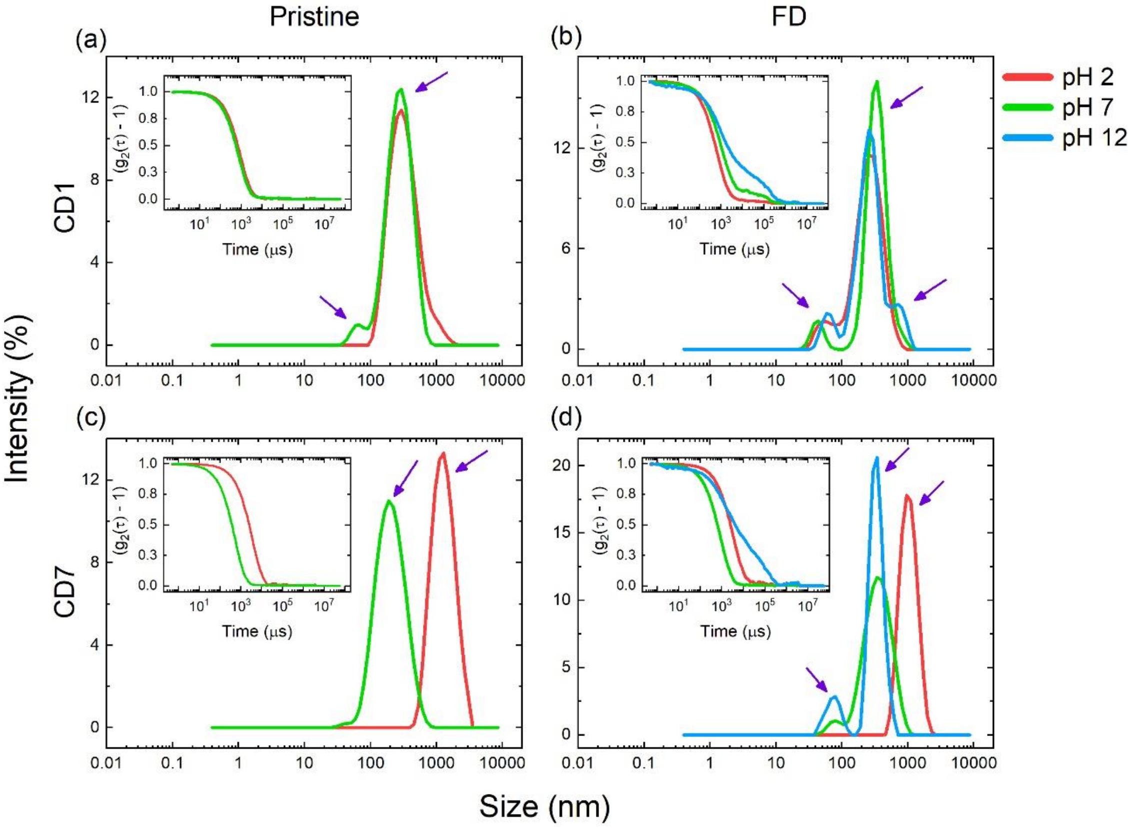

Figure 5. – DLS measurements of CDs dispersion. The dispersions were prepared in an initial 1 g·L^{-1} concentration with (a) pristine and (b) FD CD1, and with (c) pristine and (d) FD CD7 samples. The arrows indicate relevant peaks in the size distribution graphs, and the insets are the intensity correlation function $(g_2(\tau) - 1)$ for each measurement.

Due to the system's high polydispersity, the intensity correlation of the pristine N-CD dispersions prepared at pH 12 could not be resolved. But for the dispersions in other conditions, the intensity correlation could be accurately measured, as shown in the insets of Fig. 5, and the corresponding size-intensity distribution could be determined. Aggregates spanning across the size range of 150–400 nm are clearly visible, with even higher values for the FD and pristine CD7 at pH 2 (see Fig. 5(c, d)), all of which are larger than those in Tables 1 and 2.

Difference in the size distributions of the dispersions prepared with pristine and FD powder are visible as other size distribution peaks around 50–80 nm, as evidenced by the arrows in Fig. 5, particularly present for the FD samples. These objects corroborate the findings for the large aggregates in the SAXS measurements in Tables 1 and 2, and further demonstrate that the larger clusters found in SAXS are actually intermediary aggregates between the smallest clusters seen in SAXS (Fig. 4) and the largest clusters seen in the DLS (Fig. 5).

All of the data strongly suggests that the N-CDs dispersion actually consists of a complex and hierarchical cluster organization and at least three size scales are depicted using the combination of SAXS and DLS. Even more, all of these structures coexist in the dispersion and are stable due to the known surface charge mechanism of the N-CDs [39].

3.4. Centrifugation and the consequent colloidal stability

Sorting methods have already been used in CDs dispersions to separate particles by size in order to further understand their PL mechanisms and properties [37,66], making a complementary procedure for CDs preparation. In that regard, the impact of a straightforward centrifugation protocol on the morphology and structure of the dispersed N-CDs particles and aggregates is analyzed here.

Due to the improved dispersibility of N-CDs nanoparticles, other dispersions using the FD powder were prepared at an initial concentration of 30 $g{\cdot}L^{-1}$ and subjected to the centrifugation protocol discussed in Section 2.1. After centrifugation, a very small bottom body is formed in the sample holder, but the dispersions are homogeneous and their color remains the same, with no clear visual phase separation. An aliquot from the top and bottom phases was extracted after the sample centrifugation and was used for synchrotron SAXS experiments to examine the impact of centrifugation on the nanoparticle’s dispersions. Fig. 6 displays the results.

Similar conclusions to the ones discussed for the SAXS data in Fig. 4 can be traced when analyzing the curves in Fig. 6. The curve inclinations are still in the mass/surface fractal morphology regimes for CD7 and CD1, respectively, and a similar decrease in the curve inclination as pH increases is also present for the top and bottom phases of the CD7 dispersions. Furthermore, even after the centrifugation, the two level hierarchical structures are still present for most of the samples as the scattering curve shape is similar to the ones found for the non-centrifuged samples (see Figs. 3 and 4), but strickling for the top phase of the FD CD1 samples prepared in pHs 2 and 7, a substantial reduction in the scattering for the large aggregates is seen in the low-q region, and the curves resemble the form factor of a polydisperse sphere, indicating that the centrifugation was capable to separate this type of aggregates in the sample for these pH conditions, which is reasonable since in pH 2 and 7 the N-CDs have a lower surface charge [39] and consequently a lower colloidal stability, as opposed to N-CDs dispersed in pH 12, thus inducing this size separation.

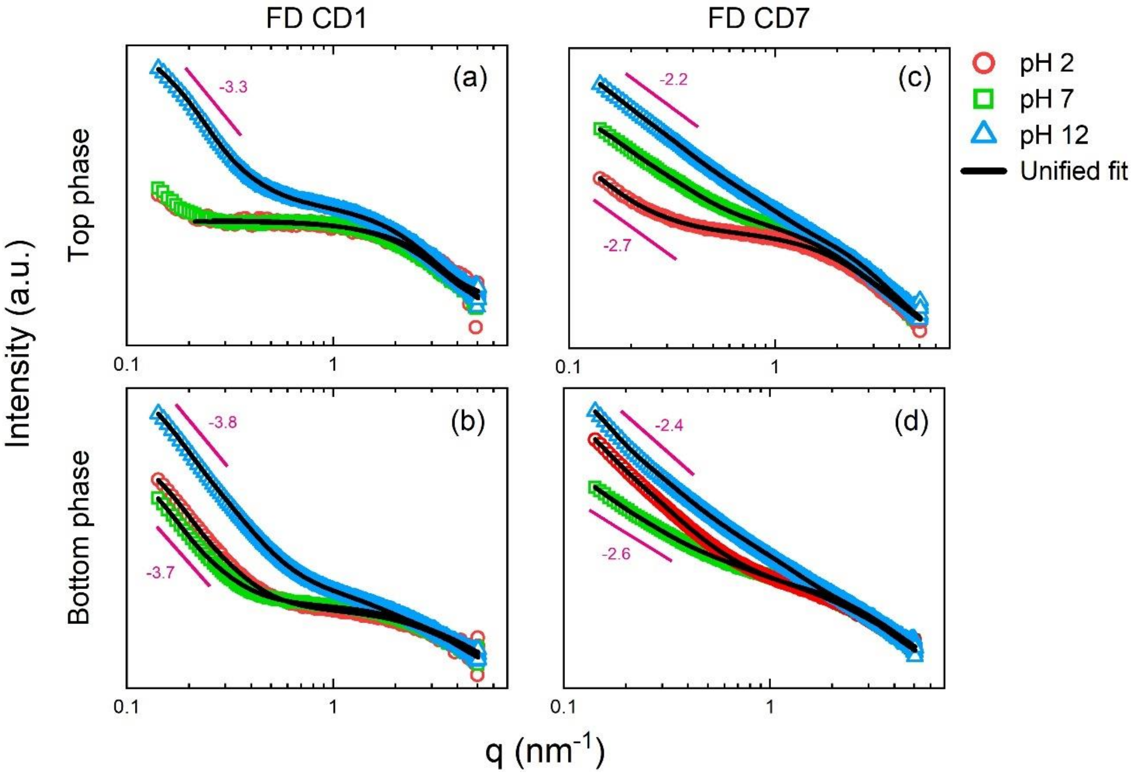

Figure 6. – Synchrotron SAXS intensity curves of the centrifuged dispersions prepared with the FD N-CDs. After the centrifugation was applied, an aliquot from the (a) top and (b) bottom phases for FD CD1 together with the (c) top and (d) bottom phases for FD CD7 were taken, all prepared at pH 2, 7, and 12 at an initial 30 g·L^{-1} concentration. The black continuous line represents the adjusted Unified fit performed on all curves, and alongside the curves a line with the corresponding inclination in the low-*q* region is displayed.

These scattering curves were again modeled using Eqs. (2) and (3) of the Unified Fit, and the resulting fits are depicted in Fig. 5. The important fit parameters obtained are displayed in Table 3 for FD CD1 and Table 4 for FD CD7.

Table 3. - Values of the large and small diameter extracted from the Unified fit for top and bottom phase of the freeze dried CD1 dispersions, prepared at an initial 30 g·L^{-1} concentration.

FD CD1 Top phase	**pH 2**	**pH 7**	**pH 12**
Large diameter (nm)	-	-	30.5 ± 0.6
Small diameter (nm)	1.57 ± 0.01	1.73 ± 0.02	1.96 ± 0.02

FD CD1 Bottom phase	pH 2	pH 7	pH 12
Large diameter (nm)	42.2 ± 0.2	47.0 ± 3.7	45.9 ± 0.8
Small diameter (nm)	1.44 ± 0.01	1.57 ± 0.02	2.75 ± 0.02

Table 4. - Values of the large and small diameter extracted from the Unified fit for top and bottom phase of the freeze dried CD7 dispersions, prepared at an initial 30 g·L^{-1} concentration.

FD CD7 Top phase	**pH 2**	**pH 7**	**pH 12**
Large diameter (nm)	40.2 ± 1.2	31.5 ± 1.3	34.6 ± 2.7
Small diameter (nm)	1.90 ± 0.01	2.19 ± 0.01	2.94 ± 0.04

FD CD7 Bottom phase	pH 2	pH 7	pH 12
Large diameter (nm)	44.2 ± 1.9	42.3 ± 2.6	44.5 ± 1.8
Small diameter (nm)	1.80 ± 0.01	3.62 ± 0.04	3.81 ± 0.03

Firstly, the average large aggregate diameter value had a small diminishing when comparing the top and bottom phases, especially for pH 7 and 12 of CD7. Overall, it is difficult to interpret such a small change since polydispersion of the large aggregates could also be present [67]. Furthermore, a similar trend to the results presented in Tables 1 and 2 can be seen here with the increase in size of the small aggregate diameter when pH is increased. For CD1 at pH 2 and 7, where the large aggregates were separated, the diameter of the smaller aggregates is equivalent to the average diameter of single N-CD sphere, even when considering the size and polydispersity of the N-CDs nanoparticles.

Finally, due to poor signal and low counting rate related to few particles in the dispersion, DLS experiments could not be conducted to the centrifuged samples, but their Zeta potential could. For that, both pristine and FD powder were used to prepare samples again in an initial 1 g·L^{-1} concentration at the three pHs considered in the previous characterization. The dispersions were also centrifuged, and the results of the Zeta potential for the top and bottom phases are shown in Fig. 7.

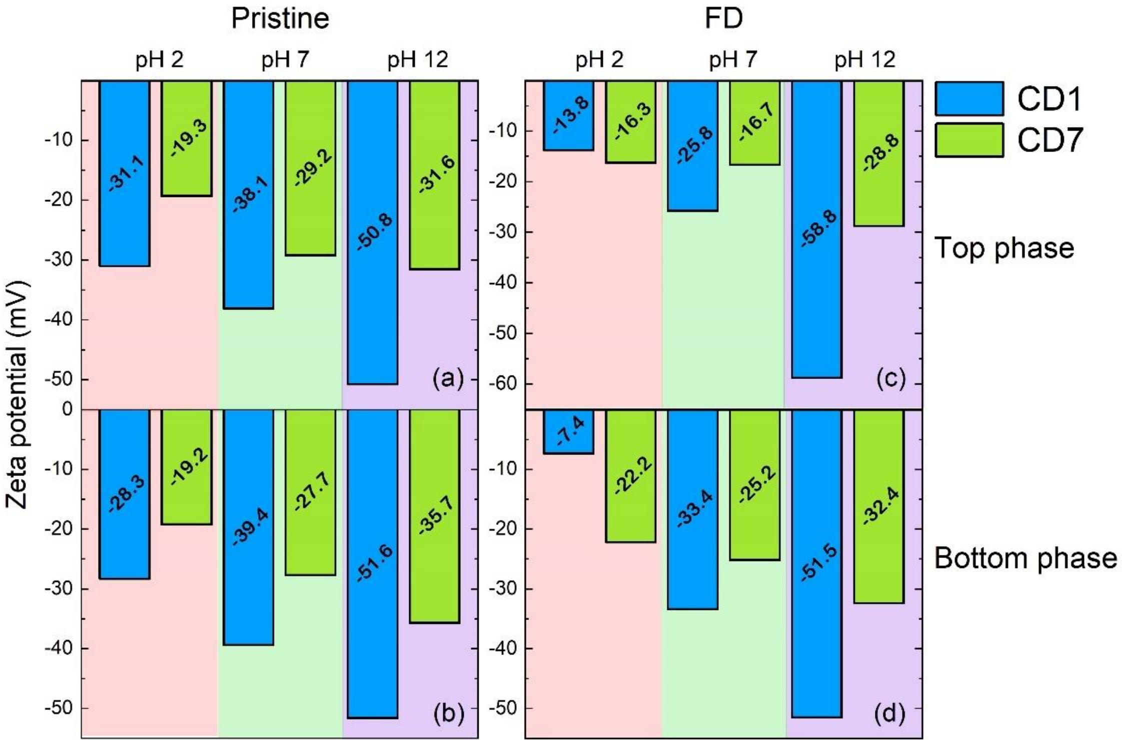

Figure 7. – Zeta potential measurements performed on the centrifuged N-CDs samples. (a) top and (b) bottom phases of the samples prepared with the pristine N-CDs powder, and (c) top and (d) bottom phases prepared with the FD N-CDs powder. All samples prepared with an initial 1 g·L^{-1} and at pHs 2, 7, and 12.

Fig. 7 further confirms that the zeta potential values for N-CDs are known to be strongly pH dependent, and the same tendency of increasing the zeta values as pH increases, seen in a previous work [39] can be seen for both top and bottom phases of CD1 and CD7. This increase in zeta values with pH is related to the deprotonation process of the carboxyl groups into carboxylate, which increases the overall negative charge of the N-CDs surface. Since more carboxyl groups are present in CD1 than in CD7, that in turn have more oxygenized nitrogen groups in its surface that don’t contribute to the overall negative charge of the nanoparticle, higher zeta potential values are found for CD1 rather than CD7, irrespective if it is the top or bottom phases of the sample.

4. Conclusion

In summary, the structural characteristics of nitrogen-rich carbon dots (N-CDs) were investigated while dispersed in an aqueous medium at different pHs of interest. Two types of N-CDs were investigated with different nitrogen-to-carbon molar ratios of 0.14 (CD1) and 0.74 (CD7). The N-CDs powder was used in two conditions: pristine being oven-dried after the synthesis and with the pristine powder being freeze-dried (FD).

First, understanding the morphology of N-CDs in aqueous media requires a detailed description of their structure in powder form. XRD further confirmed the known structure of the N-CDs, with CD1 having a hexagonal packing with an average crystallite size of (1.96 ± 0.05) nm and CD7 with a β-C_3N_4 structure and a (2.46 ± 0.03) nm crystallite size. HRTEM was also allowed to identify the individual N-CDs and validate their expected circular shape. More notably, SAXS/WAXS experiments showed a -4 inclination in the low-q region for both pristine and FD N-CDs powder, with FD samples having a larger predominance of the -4 inclination. Indicating that the N-CDs nanoparticles are aggregated in a dense matrix.

The samples were dispersed in type 1 water at three main pHs: alkaline, neutral, and acidic. Firstly, time-resolved synchrotron SAXS experiments investigated sedimentation in the dispersions prepared with pristine powder. During the time interval investigated, pH 12 samples were more stable, with little to no sedimentation occurring in the low-q region, while pH 2 samples clearly showed a decrease in the scattering intensity as time passed. The sedimentation ceased in 20 minutes for samples, and such sedimentation was described by a first-order kinetic process.

Furthermore, other synchrotron SAXS experiments were performed on both pristine and FD dispersions at different pHs, revealing two types of large aggregates. The morphology of these large aggregates is related to the nitrogen content inside each N-CD, with CD1 having a surface fractal morphology and CD7 having a mass fractal morphology. The amount of H+ and OH- influences the breakage of the nanoparticle matrix, as pH seems to be a tunable parameter of curve inclination in the low-q region. Also, the curve scattering was described using a two-level empirical model proposed by Beaucage. The results showed that size-equivalent large aggregates of roughly 42 nm are formed and are stable at all pHs investigated. In the high-q region, it was shown that the pH might have a slight tuning effect on the dispersed nanodot sizes, as the sizes of these smaller aggregates increase as pH increases. Lastly, even larger aggregates were found in DLS experiments, suggesting that complex and hierarchical aggregates are indeed present and stable in the N-CDs dispersion.

Finally, the impact of centrifugation on the morphology and structure of dispersed N-CDs particles and aggregates was also analyzed. The results showed that centrifugation was capable of separating large aggregates in the sample under certain pH conditions. The average large aggregate diameter value had a small diminishing effect when comparing the top and bottom phases, especially for pH 7 and 12. The zeta potential values for N-CDs were found to be strongly pH-dependent, with the same tendency to increase zeta values as pH increases. This increase in zeta values is related to the deprotonation process of carboxyl groups into carboxylate, which increases the overall negative charge of the N-CDs surface. Higher zeta potential values were found for CD1 than CD7, regardless of the top or bottom phases of the sample.

Bibliography References

[1] Q. Li, T.Y. Ohulchanskyy, R. Liu, K. Koynov, D. Wu, A. Best, R. Kumar, A. Bonoiu, P.N. Prasad, Photoluminescent carbon dots as biocompatible nanoprobes for targeting cancer cells in vitro, Journal of Physical Chemistry C 114 (2010) 12062–12068. https://doi.org/10.1021/JP911539R.

[2] J.B. Essner, C.H. Laber, S. Ravula, L. Polo-Parada, G.A. Baker, Pee-dots: biocompatible fluorescent carbon dots derived from the upcycling of urine, Green Chemistry 18 (2015) 243–250. https://doi.org/10.1039/C5GC02032H.

[3] H. Nie, M. Li, Q. Li, S. Liang, Y. Tan, L. Sheng, W. Shi, S.X.A. Zhang, Carbon dots with continuously tunable full-color emission and their application in ratiometric pH sensing, Chemistry of Materials 26 (2014) 3104–3112. https://doi.org/10.1021/CM5003669.

[4] L. Sciortino, A. Sciortino, R. Popescu, R. Schneider, D. Gerthsen, S. Agnello, M. Cannas, F. Messina, Tailoring the Emission Color of Carbon Dots through Nitrogen-Induced Changes of Their Crystalline Structure, Journal of Physical Chemistry C 122 (2018) 19897–19903. https://doi.org/10.1021/ACS.JPCC.8B04514.

[5] C. Kang, Y. Huang, H. Yang, X.F. Yan, Z.P. Chen, A Review of Carbon Dots Produced from Biomass Wastes, Nanomaterials 2020, Vol. 10, Page 2316 10 (2020) 2316. https://doi.org/10.3390/NANO10112316.

[6] M. Cui, S. Ren, Q. Xue, H. Zhao, L. Wang, Carbon dots as new eco-friendly and effective corrosion inhibitor, J Alloys Compd 726 (2017) 680–692. https://doi.org/10.1016/J.JALLCOM.2017.08.027.

[7] P.N. Joshi, A. Mathias, A. Mishra, Synthesis of ecofriendly fluorescent carbon dots and their biomedical and environmental applications, Materials Technology 33 (2018) 672–680. https://doi.org/10.1080/10667857.2018.1492683.

[8] A. Salinas-Castillo, M. Ariza-Avidad, C. Pritz, M. Camprubí-Robles, B. Fernández, M.J.R. Rama, A. Megia-Fernández, A. Lapresta-Fernández, F. Santoyo-Gonzalez, A. Schrott-Fischer, L.F.C. Vallveya, Carbon dots for copper detection with down and upconversion fluorescent properties as excitation sources, Chemical Communications 49 (2013) 1103–1105. https://doi.org/10.1039/C2CC36450F.

[9] J. Qu, X. Zhang, Y. Liu, Y. Xie, J. Cai, G. Zha, S. Jing, N, P-co-doped carbon dots as a dual-mode colorimetric/ratiometric fluorescent sensor for formaldehyde and cell imaging via an aminal reaction-induced aggregation process, Mikrochim Acta 187 (2020). https://doi.org/10.1007/S00604-020-04337-0.

[10] Y. Shi, W. Su, F. Yuan, T. Yuan, X. Song, Y. Han, S. Wei, Y. Zhang, Y. Li, X. Li, L. Fan, Carbon Dots for Electroluminescent Light-Emitting Diodes: Recent Progress and Future Prospects, Advanced Materials 35 (2023). https://doi.org/10.1002/adma.202210699.

[11] S. Qu, X. Liu, X. Guo, M. Chu, L. Zhang, D. Shen, Amplified spontaneous green emission and lasing emission from carbon nanoparticles, Adv Funct Mater 24 (2014) 2689–2695. https://doi.org/10.1002/ADFM.201303352.

[12] J. Liu, S. Lu, Q. Tang, K. Zhang, W. Yu, H. Sun, B. Yang, One-step hydrothermal synthesis of photoluminescent carbon nanodots with selective antibacterial activity against Porphyromonas gingivalis, Nanoscale 9 (2017) 7135–7142. https://doi.org/10.1039/C7NR02128C.

[13] S. Zhu, Q. Meng, L. Wang, J. Zhang, Y. Song, H. Jin, K. Zhang, H. Sun, H. Wang, B. Yang, Highly Photoluminescent Carbon Dots for Multicolor Patterning, Sensors, and Bioimaging, Angewandte Chemie International Edition 52 (2013) 3953–3957. https://doi.org/10.1002/ANIE.201300519.

[14] N. Farshidfar, S. Fooladi, M.H. Nematollahi, S. Iravani, Carbon dots with tissue engineering and regenerative medicine applications., RSC Adv 13 (2023) 14517–14529. https://doi.org/10.1039/d3ra02336b.

[15] G. Nocito, G. Calabrese, S. Forte, S. Petralia, C. Puglisi, M. Campolo, E. Esposito, S. Conoci, Carbon Dots as Promising Tools for Cancer Diagnosis and Therapy, Cancers 2021, Vol. 13, Page 1991 13 (2021) 1991. https://doi.org/10.3390/CANCERS13091991.

[16] C. Hu, M. Li, J. Qiu, Y.P. Sun, Design and fabrication of carbon dots for energy conversion and storage, Chem Soc Rev 48 (2019) 2315–2337. https://doi.org/10.1039/c8cs00750k.

[17] C. Campalani, E. Cattaruzza, S. Zorzi, A. Vomiero, S. You, L. Matthews, M. Capron, C. Mondelli, M. Selva, A. Perosa, Biobased Carbon Dots: From Fish Scales to

Photocatalysis, Nanomaterials 2021, Vol. 11, Page 524 11 (2021) 524. https://doi.org/10.3390/NANO11020524.

[18] M. Fang, B. Wang, X. Qu, S. Li, J. Huang, J. Li, S. Lu, N. Zhou, State-of-the-art of biomass-derived carbon dots: Preparation, properties, and applications, Chinese Chemical Letters 35 (2024). https://doi.org/10.1016/J.CCLET.2023.108423.

[19] F. Messina, L. Sciortino, R. Popescu, A.M. Venezia, A. Sciortino, G. Buscarino, S. Agnello, R. Schneider, D. Gerthsen, M. Cannas, F.M. Gelardi, Fluorescent nitrogen-rich carbon nanodots with an unexpected β-C3N4 nanocrystalline structure, J Mater Chem C Mater 4 (2016) 2598–2605. https://doi.org/10.1039/C5TC04096E.

[20] J. Manioudakis, F. Victoria, C.A. Thompson, L. Brown, M. Movsum, R. Lucifero, R. Naccache, Effects of nitrogen-doping on the photophysical properties of carbon dots, J Mater Chem C Mater 7 (2019) 853–862. https://doi.org/10.1039/C8TC04821E.

[21] L. Cui, X. Ren, M. Sun, H. Liu, L. Xia, Carbon Dots: Synthesis, Properties and Applications., Nanomaterials (Basel) 11 (2021). https://doi.org/10.3390/nano11123419.

[22] J. Liu, R. Li, B. Yang, Carbon Dots: A New Type of Carbon-Based Nanomaterial with Wide Applications, ACS Cent Sci 6 (2020) 2179–2195. https://doi.org/10.1021/ACSCENTSCI.0C01306.

[23] A. Sciortino, M. Gazzetto, G. Buscarino, R. Popescu, R. Schneider, G. Giammona, D. Gerthsen, E.J. Rohwer, N. Mauro, T. Feurer, A. Cannizzo, F. Messina, Disentangling size effects and spectral inhomogeneity in carbon nanodots by ultrafast dynamical hole-burning, Nanoscale 10 (2018) 15317–15323. https://doi.org/10.1039/C8NR02953A.

[24] K. Jiang, S. Sun, L. Zhang, Y. Lu, A. Wu, C. Cai, H. Lin, Red, Green, and Blue Luminescence by Carbon Dots: Full-Color Emission Tuning and Multicolor Cellular Imaging, Angewandte Chemie International Edition 54 (2015) 5360–5363. https://doi.org/10.1002/ANIE.201501193.

[25] Y.H. Yuan, Z.X. Liu, R.S. Li, H.Y. Zou, M. Lin, H. Liu, C.Z. Huang, Synthesis of nitrogen-doping carbon dots with different photoluminescence properties by controlling the surface states, Nanoscale 8 (2016) 6770–6776. https://doi.org/10.1039/C6NR00402D.

[26] Y. Ru, G.I.N. Waterhouse, S. Lu, Aggregation in carbon dots, Aggregate 3 (2022) e296. https://doi.org/10.1002/AGT2.296.

[27] X. Ma, R. Sun, J. Cheng, J. Liu, F. Gou, H. Xiang, X. Zhou, Fluorescence Aggregation-Caused Quenching versus Aggregation-Induced Emission: A Visual Teaching Technology for Undergraduate Chemistry Students, J Chem Educ 93 (2016) 345–350. https://doi.org/10.1021/ACS.JCHEMED.5B00483.

[28] C. Kang, S. Tao, F. Yang, B. Yang, Aggregation and luminescence in carbonized polymer dots, Aggregate 3 (2022). https://doi.org/10.1002/AGT2.169.

[29] S. Lee, J. Lee, S. Jeon, Aggregation-induced emission of matrix-free graphene quantum dots via selective edge functionalization of rotor molecules, Sci Adv 9 (2023). https://doi.org/10.1126/SCIADV.ADE2585.

[30] W. Li, S. Wu, X. Xu, J. Zhuang, H. Zhang, X. Zhang, C. Hu, B. Lei, C.F. Kaminski, Y. Liu, Carbon Dot-Silica Nanoparticle Composites for Ultralong Lifetime Phosphorescence Imaging in Tissue and Cells at Room Temperature, Chemistry of Materials 31 (2019) 9887–9894. https://doi.org/10.1021/ACS.CHEMMATER.9B04120.

[31] Z. Tian, X. Zhang, D. Li, D. Zhou, P. Jing, D. Shen, S. Qu, R. Zboril, A.L. Rogach, Full-Color Inorganic Carbon Dot Phosphors for White-Light-Emitting Diodes, Adv Opt Mater 5 (2017). https://doi.org/10.1002/ADOM.201700416.

[32] F. Arshad, A. Pal, M.P. Sk, Review—Aggregation-Induced Emission in Carbon Dots for Potential Applications, ECS Journal of Solid State Science and Technology 10 (2021) 021001. https://doi.org/10.1149/2162-8777/ABDFB8.

[33] Z.X. Liu, Z.L. Wu, M.X. Gao, H. Liu, C.Z. Huang, Carbon dots with aggregation induced emission enhancement for visual permittivity detection, Chemical Communications 52 (2016) 2063–2066. https://doi.org/10.1039/C5CC08635C.

[34] T. Li, A.J. Senesi, B. Lee, Small Angle X-ray Scattering for Nanoparticle Research, Chem Rev 116 (2016) 11128–11180. https://doi.org/10.1021/ACS.CHEMREV.5B00690/ASSET/IMAGES/CR-2015-00690Z_M061.GIF.

[35] F. Rigodanza, M. Burian, F. Arcudi, L. Đorđević, H. Amenitsch, M. Prato, Snapshots into carbon dots formation through a combined spectroscopic approach, Nature Communications 2021 12:1 12 (2021) 1–9. https://doi.org/10.1038/s41467-021-22902-w.

[36] S. Qu, X. Wang, Q. Lu, X. Liu, L. Wang, A Biocompatible Fluorescent Ink Based on Water-Soluble Luminescent Carbon Nanodots, Angewandte Chemie International Edition 51 (2012) 12215–12218. https://doi.org/10.1002/ANIE.201206791.

[37] A. Sciortino, N. Mauro, G. Buscarino, L. Sciortino, R. Popescu, R. Schneider, G. Giammona, D. Gerthsen, M. Cannas, F. Messina, β-C3N4 Nanocrystals: Carbon Dots with Extraordinary Morphological, Structural, and Optical Homogeneity, Chemistry of Materials 30 (2018) 1695–1700. https://doi.org/10.1021/acs.chemmater.7b05178.

[38] F. Messina, L. Sciortino, G. Buscarino, S. Agnello, F. Gelardi, M. Cannas, Photoluminescence of Carbon Dots Embedded in a SiO2 Matrix, Mater Today Proc 3 (2016) S258–S265. https://doi.org/10.1016/J.MATPR.2016.02.043.

[39] T. Fiuza, G. Gomide, A. Fabiano, C. Campos, F. Messina, J. Depeyrot, On the Colloidal Stability of Nitrogen-Rich Carbon Nanodots Aqueous Dispersions, C 2019, Vol. 5, Page 74 5 (2019) 74. https://doi.org/10.3390/C5040074.

[40] T. Fiuza, L. Da Silva, Ferrofluidos e Dots de Carbono como exemplos de nanomateriais multifuncionais para a conversão de energia, (2020). http://repositorio2.unb.br/jspui/handle/10482/41135 (accessed May 25, 2024).

[41] C.B. Carter, D.B. Williams, Transmission electron microscopy: Diffraction, imaging, and spectrometry, 2016. https://doi.org/10.1007/978-3-319-26651-0.

[42] A.S. Aguiar, Síntese de nanopartículas magnéticas em dispersões de Laponita : um estudo da hidrofilicidade, (2020). http://repositorio2.unb.br/jspui/handle/10482/40200 (accessed May 25, 2024).

[43] S.R.S. Bernard Dennis Cullity, Elements of X-ray diffraction, 3rd edition, 3rd, illustr ed., Prentice Hall, 2001. https://doi.org/citeulike-article-id:3998040.

[44] J. Als-Nielsen, D. McMorrow, Elements of modern X-ray physics, Phys Today 55 (2002) 63. https://doi.org/10.1063/1.1472397.

[45] B.Eugene. Warren, X-ray diffraction, Dover publication, 1990. https://books.google.com.br/books?hl=en&lr=&id=wfLBhAbEYAsC&oi=fnd&pg=PA1&dq=x+ray+diffraction&ots=QHPnNHbwkN&sig=O6_QYcOLSVnx9RV4gg4_wlm5h_8&redir_esc=y#v=onepage&q=x ray diffraction&f=false (accessed June 5, 2019).

[46] B.R. Pauw, Everything SAXS: Small-angle scattering pattern collection and correction, Journal of Physics Condensed Matter 25 (2013). https://doi.org/10.1088/0953-8984/25/38/383201.

[47] N. Stribeck, X-Ray Scattering of Soft Matter, X-Ray Scattering of Soft Matter (2007). https://doi.org/10.1007/978-3-540-69856-2.

[48] G. Beaucage, IUCr, Approximations Leading to a Unified Exponential/Power-Law Approach to Small-Angle Scattering, Urn:Issn:0021-8898 28 (1995) 717–728. https://doi.org/10.1107/S0021889895005292.

[49] D.J. Pochapski, C. Carvalho Dos Santos, G.W. Leite, S.H. Pulcinelli, C.V. Santilli, Zeta Potential and Colloidal Stability Predictions for Inorganic Nanoparticle Dispersions: Effects of Experimental Conditions and Electrokinetic Models on the Interpretation of Results, Langmuir 37 (2021) 13379–13389. https://doi.org/10.1021/acs.langmuir.1c02056.

[50] V. Mackert, M.A. Schroer, M. Winterer, Unraveling agglomeration and deagglomeration in aqueous colloidal dispersions of very small tin dioxide nanoparticles, J Colloid Interface Sci 608 (2022) 2681–2693. https://doi.org/10.1016/j.jcis.2021.10.194.

[51] D. Tang, Y. Zhao, D. Han, Y. Xie, Microstructure of virgin and aged asphalts by small-angle X-ray scattering, Case Studies in Construction Materials 19 (2023) e02578. https://doi.org/10.1016/J.CSCM.2023.E02578.

[52] R. Pecora, Dynamic light scattering measurement of nanometer particles in liquids, Journal of Nanoparticle Research 2 (2000) 123–131. https://doi.org/10.1023/A:1010067107182/METRICS.

[53] K.J. Mintz, M. Bartoli, M. Rovere, Y. Zhou, S.D. Hettiarachchi, S. Paudyal, J. Chen, J.B. Domena, P.Y. Liyanage, R. Sampson, D. Khadka, R.R. Pandey, S. Huang, C.C. Chusuei, A. Tagliaferro, R.M. Leblanc, A deep investigation into the structure of carbon dots, Carbon N Y 173 (2021) 433–447. https://doi.org/10.1016/J.CARBON.2020.11.017.

[54] I. Diwan, G.K. Tripathi, P.S. Khare, Synthesis of green fluorescent, energy efficient nitrogen doped carbon quantum dots, Optik (Stuttg) 303 (2024). https://doi.org/10.1016/j.ijleo.2024.171725.

[55] C.M. Ferreira, G.J. da Silva, Absorption of essential oils in Laponite: Stability enhancement and structural characteristics, Appl Clay Sci 238 (2023). https://doi.org/10.1016/j.clay.2023.106936.

[56] O. Spalla, S. Lyonnard, F. Testard, Analysis of the small-angle intensity scattered by a porous and granular medium, Urn:Issn:0021-8898 36 (2003) 338–347. https://doi.org/10.1107/S0021889803002279.

[57] E.A. Chavez Panduro, T. Beuvier, M. Fernández Martínez, L. Hassani, B. Calvignac, F. Boury, A. Gibaud, Small-angle X-ray scattering analysis of porous powders of CaCO3, Urn:Issn:0021-8898 45 (2012) 881–889. https://doi.org/10.1107/S0021889812032219.

[58] D. Saurel, J. Segalini, M. Jauregui, A. Pendashteh, B. Daffos, P. Simon, M. Casas-Cabanas, A SAXS outlook on disordered carbonaceous materials for electrochemical energy storage, Energy Storage Mater 21 (2019) 162–173. https://doi.org/10.1016/J.ENSM.2019.05.007.

[59] Indriyati, M.M. Munir, M. Nasir, F. Iskandar, Effect of post-treatment drying processes on the optical and photothermal properties of carbon nanodots derived via microwave-assisted method, IOP Conf Ser Earth Environ Sci 1017 (2022) 012009. https://doi.org/10.1088/1755-1315/1017/1/012009.

[60] E. Trenkenschuh, W. Friess, Freeze-drying of nanoparticles: How to overcome colloidal instability by formulation and process optimization, European Journal of Pharmaceutics and Biopharmaceutics 165 (2021) 345–360. https://doi.org/10.1016/j.ejpb.2021.05.024.

[61] F. Xie, Z. Xu, A.C.S. Jensen, F. Ding, H. Au, J. Feng, H. Luo, M. Qiao, Z. Guo, Y. Lu, A.J. Drew, Y.S. Hu, M.M. Titirici, Unveiling the role of hydrothermal carbon dots as anodes in sodium-ion batteries with ultrahigh initial coulombic efficiency, J Mater Chem A Mater 7 (2019) 27567–27575. https://doi.org/10.1039/c9ta11369j.

[62] H. Li, X. He, Y. Liu, H. Huang, S. Lian, S.T. Lee, Z. Kang, One-step ultrasonic synthesis of water-soluble carbon nanoparticles with excellent photoluminescent properties, Carbon N Y 49 (2011) 605–609. https://doi.org/10.1016/J.CARBON.2010.10.004.

[63] H. Li, X. He, Z. Kang, H. Huang, Y. Liu, J. Liu, S. Lian, C.H.A. Tsang, X. Yang, S.T. Lee, Water-Soluble Fluorescent Carbon Quantum Dots and Photocatalyst Design, Angewandte Chemie International Edition 49 (2010) 4430–4434. https://doi.org/10.1002/ANIE.200906154.

[64] G. Beaucage, Combined Small-Angle Scattering for Characterization of Hierarchically Structured Polymer Systems over Nano-to-Micron Meter: Part II Theory, Polymer Science: A Comprehensive Reference: Volume 1-10 1–10 (2012) 399–409. https://doi.org/10.1016/B978-0-444-53349-4.00032-7.

[65] W.J. Ong, L.L. Tan, S.P. Chai, S.T. Yong, A.R. Mohamed, Surface charge modification via protonation of graphitic carbon nitride (g-C3N4) for electrostatic self-assembly construction of 2D/2D reduced graphene oxide (rGO)/g-C3N4 nanostructures toward enhanced photocatalytic reduction of carbon dioxide to methane, Nano Energy 13 (2015) 757–770. https://doi.org/10.1016/J.NANOEN.2015.03.014.

[66] N. Stribeck, Interpretation of Scattering Patterns, X-Ray Scattering of Soft Matter (2007) 95–190. https://doi.org/10.1007/978-3-540-69856-2_8.

[67] E.M. Anitas, Small-Angle Scattering from Fractals: Differentiating between Various Types of Structures, Symmetry (Basel) 12 (2020) 65. https://doi.org/10.3390/sym12010065.

[68] E.M. Anitas, Small-Angle Scattering from Mass and Surface Fractals, Complexity in Biological and Physical Systems - Bifurcations, Solitons and Fractals (2018). https://doi.org/10.5772/INTECHOPEN.70870.

[69] M.S. Gatto, W. Najahi-Missaoui, Lyophilization of Nanoparticles, Does It Really Work? Overview of the Current Status and Challenges, Int J Mol Sci 24 (2023). https://doi.org/10.3390/IJMS241814041.

[70] G. Beaucage, Small-angle scattering from polymeric mass fractals of arbitrary mass-fractal dimension, J Appl Crystallogr 29 (1996) 134–146. https://doi.org/10.1107/S0021889895011605.

[71] T.P. Rieker, S. Misono, F. Ehrburger-Dolle, Small-angle X-ray scattering from carbon blacks: Crossover between the fractal and porod regimes, Langmuir 15 (1999) 914–917. https://doi.org/10.1021/LA981280N.

[72] L. Deng, X. Wang, Y. Kuang, C. Wang, L. Luo, F. Wang, X. Sun, Development of hydrophilicity gradient ultracentrifugation method for photoluminescence investigation of separated non-sedimental carbon dots, Nano Res 8 (2015) 2810–2821. https://doi.org/10.1007/S12274-015-0786-Y/METRICS.

[73] G. Beaucage, H.K. Kammler, S.E. Pratsinis, Particle size distributions from small-angle scattering using global scattering functions, Urn:Issn:0021-8898 37 (2004) 523–535. https://doi.org/10.1107/S0021889804008969.